Enantiospecific state transfer on a tight lower bound of energy-time costs

Min-Peng Han,[1] Libin Fu,[1,*] and Chong Ye[2,†]
[1]*Graduate School of China Academy of Engineering Physics, Beijing 100193, China*
[2]*Beijing Key Laboratory of Nanophotonics and Ultrafine Optoelectronic Systems, School of Physics, Beijing Institute of Technology, Beijing 100081, China*

(Received 13 January 2026; accepted 18 March 2026; published 14 April 2026)

Enantiospecific state transfer is a special quantum control problem whose importance is emphasized due to its potential applications in enantiodetection and enantioseparation. However, crucial discussions about obtaining highly efficient enantiospecific state transfer working on the tight lower bound of energy-time costs were missing. Here, we establish a frame to systematically study this issue by mapping the control protocol to the curve in the parameter space that is determined by the evolution of control fields and the efficiency of enantiospecific state transfer. We derive a tight lower bound on the conjoint costs, considering factors such as time, energy input from control fields, and the efficiency of enantiospecific state transfer. This leads to the formulation of a different criterion for evaluating and improving enantiospecific state transfer techniques. Furthermore, we present an optimal approach for implementing highly efficient control protocols with minimal time-energy expenditure.

DOI: 10.1103/zstx-lxm8

I. INTRODUCTION

Enantiospecific state transfer (ESST) [1–3] is a special quantum control problem [4–8]. It aims to control the chiral molecules of opposite chirality from the same energetic state to different energetic states. The importance of ESST is emphasized due to its potential applications in enantiodetection and enantioseparation. While enantiomers of opposite handednesses share almost identical physical properties, such as melting and boiling points, their functions in broad classes of chemical reactions and biological activity change dramatically with their handedness [9–11]. Therefore, enantiodetection and enantioseparation of chiral mixtures are among the most important and challenging tasks in natural science [12–15]. When perfect ESST is achieved in chiral mixtures, enantiomers of opposite handednesses can be distinguished [16] and even separated via energy-dependent technologies. Besides this, the combination of ESST and Ramsey spectroscopy has potential advantages in observing parity violation in chiral mixtures [17].

To obtain highly efficient ESST, Shapiro *et al.* [18–21] proposed the cyclic three-level (CTL) model of chiral molecules, where transition electric dipoles change signs with handednesses due to the breaking of the inversion symmetry in chiral molecules. This feature makes it possible to yield strongly enantioselective responses in the electric dipole approximation [22–33]. In contrast, relatively weak magnetic dipole and electric quadrupole interactions were needed in traditional chiroptical methods [1–3,12–15], resulting in weakly enantioselective responses and limiting the realization of ESST. Therefore, the chiroptical methods based on the CTL model offer promising alternative solutions for the related issues.

The time cost and energy input of the control protocols are essentially important in ESST experiments [34–37]. The pioneer ESST methods based on the CTL model [18–21] required time-consuming adiabatic passage and thus were not experimentally realized. This motivated the introduction of polyatomic-molecule cooling technologies [38–40] and fast quantum control technologies in ESST, such as the short-pulse methods [41–46], the shortcut-to-adiabatic methods [47,48], and so on [49–56].

The energy cost, regardless of its definition, is of great interest in quantum control problems [57–63]. In ESST, the energy input of the driving fields is a natural definition of energy cost. On the one hand, it is limited by the ability of field generators. On the other hand, it is directly related to the harmful heat loads [39], which can increase the system's temperature and reduce decoherence time. These limit the efficiency of ESST in buffer gas cells [34]. Therefore, finding the optimal protocols of ESST with minimal energy-time cost and high efficiency is of significant importance.

Moreover, it is of greatest interest to give a criterion, in the form of a lower bound of time-energy cost [64–67], for assessing and refining the control protocols in quantum control problems. Providing a criterion on time-energy cost is also important in ESST because it is a quantum control problem. However, ESST is different from the usual quantum control problems. In ESST, two quantum species are controlled simultaneously, and their difference in the final states is important rather than the final states themselves. In contrast, in the usual quantum control problems, only one quantum species is controlled, and the final state itself is important. Then, the efficiency of ESST is measured by the enantiomeric enrichment in a selected energetic state. Thus, it is natural to explore the lower bound of ESST on the conjoint cost, considering factors such as time, energy input from control fields, and efficiency, and provide an approach for implementing highly efficient control protocols with minimal time-energy cost.

*Contact author: lbfu@gscaep.ac.cn
†Contact author: yechong@bit.edu.cn

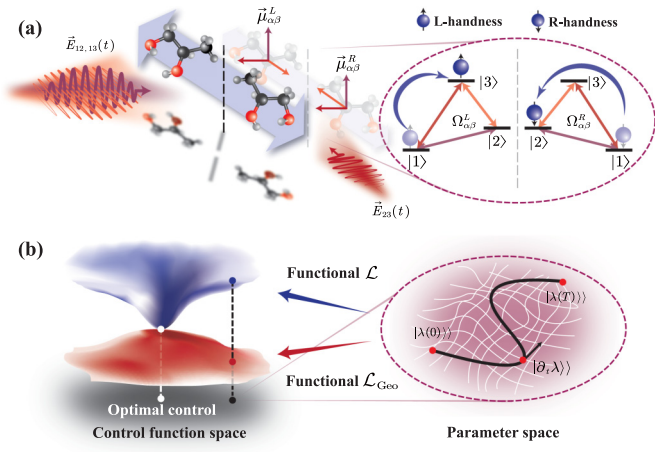

FIG. 1. (a) The CTL model, including its implementation and its enantioselectivity in the electric transition dipoles $\vec{\mu}_{\alpha\beta}$, and an example of highly efficient ESST. (b) Our geometric approach. A control protocol gives rise to a curve in the parameter space of $|\lambda\rangle\rangle$. The conjoint costs are related to the velocity vector $|\partial_t\lambda\rangle\rangle$ and are numerically minimized to obtain optimal control. The curve length gives the tight lower bound $\mathcal{L}_{\rm Geo}$ for the conjoint costs.

In this paper, we develop a framework to systematically study these two problems. To this end, we define time-dependent vectors concerning the evolution of control fields and the efficiency of ESST. These vectors form a parameter space. A control protocol will result in a curve in the parameter space. With the help of this geometric frame, we prove that the length of the curve sets a tight lower bound on the conjoint cost concerning the operation time, overall energy input, and efficiency of ESST. That is to say, we find the lower bound of the time-energy cost for ESST. Further, we verify the lower bound is tight. Following quantum optimal control theories, we establish a scheme to obtain highly efficient control protocols with minimal time-energy cost. The time-energy cost is approximately two times more energy efficient than the current method. We further discuss the applications in typical experimental environments and analyze its robustness against systematic errors.

II. THEORETICAL FRAMEWORK

A. Enantiospecific state transfer in cyclic three-level model

We discuss ESST in the cyclic three-level (CTL) model of chiral molecules in the three-photon resonance condition as shown in Fig. 1(a). In the rotating-wave approximation, the general Hamiltonians of the left- and right-handed molecules are given as ($\hbar = 1$)

$$H^Q = \sum_{\alpha=2,3} \Delta_{\alpha 1}|\alpha\rangle_Q\langle\alpha| + \sum_{\alpha>\beta=1}^{3} \frac{1}{2}\left(\Omega^Q_{\alpha\beta}|\alpha\rangle_Q\langle\beta| + \text{H.c.}\right), \tag{1}$$

where the subscript $Q(= L, R)$ denotes the handedness of the molecules. The complex coupling strengths are given as $\Omega^{L/R}_{\alpha\beta} = \mu^{L/R}_{\alpha\beta}E_{\alpha\beta}(t)/\hbar$. Compared with other parameters, the tiny parity-violation energy differences between left- and right-handed molecules are negligible [17], and thus the detunings $\Delta_{\alpha 1}$ are not enantioselective. Due to the intrinsic chirality of chiral molecules, the electric transition dipoles change signs with enantiomers (i.e., $\mu^L_{\alpha\beta} = -\mu^R_{\alpha\beta} = \mu_{\alpha\beta}$), and so do the complex coupling strengths

$$\Omega^L_{\alpha\beta} = -\Omega^R_{\alpha\beta} = \Omega_{\alpha\beta}. \tag{2}$$

In ESST [18–21,41–56], the goal is to design control protocols maximizing the enantiomeric enrichment in a selected state $|\varepsilon_\alpha|$ ($\alpha = 1, 2, 3$) with

$$\varepsilon_\alpha \equiv |\langle\alpha|\psi^L(T)\rangle_L|^2 - |\langle\alpha|\psi^R(T)\rangle_R|^2, \tag{3}$$

where T is the overall operation time and $|\psi^Q(T)\rangle_Q$ are the final states of the two enantiomers. While effects of the decoherence, the Doppler shift, thermal populations, couplings to the states outside the working model, and other real factors change case by case in experiments, the Schrödinger equations of chiral molecules based on Eq. (1) are fixed by the control fields. For convenience, the ideal conditions are usually assumed and thus, the control protocols are usually designed based on the perfect initial states $\hat{\rho}_0 = \sum_{Q=L,R} c_Q|1\rangle_Q\langle 1|$ and the Schrödinger equation [18–21,41–56].

B. Energy and time cost of enantiospecific state transfer

Beyond the efficiency, the time and energy costs of the control are of great interest. In quantum optimal control theory [61–63], the energy cost can be defined as the overall input energy of the control, which does not depend on the interaction between the controls and the quantum items. Following this spirit, we have

$$\mathscr{E}_{\rm total}(T) \equiv \sum_{\alpha>\beta=1}^{3} \int_0^T |E_{\alpha\beta}(t)|^2 dt. \tag{4}$$

The energy cost can also be defined as the Frobenius norms related to the interactions between the controls and the quantum items [64–67]. Although these two definitions are different in our discussions, they become the same in some specific cases. The time cost of the enantiospecific state transfer is simple, which is given by the operation time of the control protocols (i.e., T).

C. Geometric bound of ESST on energy-time cost and efficiency

ESST is different from the common quantum control problems. To see this, we give the possible perfect ESST processes with $\varepsilon_3 = 1$,

$$\hat{\rho}_0 = \sum_{Q=L,R} c_Q|1\rangle_Q\langle 1| \to \hat{\rho}_f = c_L|3\rangle_L\langle 3| + c_R|\psi\rangle_R\langle\psi|. \tag{5}$$

The final state $|\psi\rangle_R$ is unfixed and is only constrained by $\langle 3|\psi\rangle_R = 0$. It is clearly shown that ESST is dual-objective with unfixed target states, which strongly departs from the common quantum control problems that are single-objective with fixed target states [64–67].

To obtain the lower bound of the energy-time cost in ESST, we develop a geometric frame as shown in Fig. 1(b). We construct a parameter space formed by four-dimensional vectors

$|\lambda\rangle\rangle = [\lambda_1, \lambda_2, \lambda_3, \lambda_4]^{\mathrm{T}}$ defined as

$$|\lambda(t)\rangle\rangle \equiv \int_0^t [\epsilon, E_{12}(t'), E_{13}(t'), E_{23}(t')]^{\mathrm{T}} dt' \tag{6}$$

with $\epsilon \equiv \sqrt{1-|\varepsilon_3|}$. The inner product is defined as $\langle\langle \lambda, \lambda\rangle\rangle \equiv \sum_{\mu,\nu=1}^{4} g_{\mu\nu}\lambda_\mu^*\lambda_\nu$ with the positive metric of $g_{\mu\nu} = \mathrm{diag}(\zeta, \xi, \xi, \xi)$ ($\{\zeta, \xi\} > 0$). When applying a control protocol to the left- and right-handed molecules, we obtain a curve in the parameter space, whose length is given as

$$\mathscr{L}_{\mathrm{Geo}} = \int_0^T \sqrt{\sum_{\mu,\nu=1}^{4} g_{\mu\nu}(\partial_t\lambda_\mu^*)(\partial_t\lambda_\nu)}dt. \tag{7}$$

In our geometric frame, the conjoint cost of the time cost, the energy cost, and the ESST efficiency is defined as

$$\mathcal{L} \equiv \int_0^T \langle\langle \partial_t\lambda, \partial_t\lambda\rangle\rangle dt = \zeta(1-|\varepsilon_3|)T + \xi\mathscr{E}_{\mathrm{total}}. \tag{8}$$

Then, the time cost, the energy cost, and the ESST efficiency of the control protocol are embedded in $\mathcal{L}$. We can use the Cauchy-Schwarz inequality to Eq. (8). The Cauchy-Schwarz inequality tells

$$\left[\int_0^T f^2(t)dt\right]\left[\int_0^T g^2(t)dt\right] \geqslant \left[\int_0^T f(t)g(t)dt\right]^2. \tag{9}$$

Applying it to Eq. (7) by adopting $f(t) = \sqrt{\langle\langle \partial_t\lambda, \partial_t\lambda\rangle\rangle}$ and $g(t) = 1$, we have

$$\left(\int_0^T \langle\langle \partial_t\lambda, \partial_t\lambda\rangle\rangle dt\right)\left(\int_0^T dt\right) \geqslant \left[\int_0^T dt\sqrt{\langle\langle \partial_t\lambda, \partial_t\lambda\rangle\rangle}\right]^2. \tag{10}$$

Then, we arrive at

$$\mathcal{L} \geqslant \frac{1}{T}\left(\int_0^T \sqrt{\sum_{\mu,\nu=1}^{4} g_{\mu\nu}(\partial_t\lambda_\mu^*)(\partial_t\lambda_\nu)}dt\right)^2 \equiv \frac{\mathscr{L}_{\mathrm{Geo}}^2}{T}. \tag{11}$$

We will show that the bound in Eq. (11) is tight. The positive metric $g_{\mu\nu}$ is related to the non-negative weight that can be changed to improve the resulting balance among the three key elements. Thus, it establishes the basic limitations on the quantum control of ESST based on CTL models and can serve as a benchmark for assessing and refining ESST techniques.

D. Quantum optimal control approach

In our framework, we also obtain the quantum optimal protocols by minimizing the conjoint cost $\mathcal{L}$ with the help of standard quantum optimal control (QOC) theories [59–62]. The QOC theories have been widely used in quantum control tasks such as quantum computing [61], quantum sensing [61], quantum battery [62,63], and molecular orientations [68–71]. We expand its application into enantiospecfic state transfer. Hereafter, the protocols delivered from the QOC approach will be distinguished from others as QOC protocols. They are technologically important as they have the lowest time-energy consumption. Moreover, with the help of QOC protocols, we can answer whether the lower bound in Eq. (11) is tight, which is the key interest of our discussions. Specifically, the QOC approach of ESST is implemented as follows.

Firstly, we determine the control parameters. One of the important elements for a control protocol is the pulse shape of each field, i.e., the time evolution of the amplitude $E_{\alpha\beta}^{\mathrm{amp}}(t)$ ($3 \geqslant \beta > \alpha \geqslant 1$). Beyond the pulse shapes, the detunings (i.e., Δ_{31} and Δ_{21}) and the relative phase ($\phi \equiv \phi_{12} + \phi_{23} - \phi_{13}$ with $\phi_{\alpha\beta} \equiv \arg(\Omega_{\alpha\beta})$) are essentially important. For perfect ESSTs, there are two special solutions of the detunings and the relative phase, i.e., $\Delta_{31} = \Delta_{21} \equiv \Delta = 0$ and $\phi = \pm\pi/2$, which were widely used [35–37,41–43,47–51,54–56] and even analytically given [36,41,43,51]. Typically, the analytical derivation assumes that the three pulses are separated (nonoverlapping). However, our model addresses a more generalized scenario that does not rely on this assumption, which complicates the analytical derivation of phase relationships. In addition, there were other solutions of Δ and ϕ for perfect ESSTs [18,20,44,45,55]. Importantly, we aim to find protocols for simultaneously obtaining high efficiency and low energy cot. In this context, the control protocols of ESST can be described as

$$\mathbb{F} \equiv \left\{\left\{E_{\alpha\beta}^{\mathrm{amp}}(t), \Delta_{21}, \Delta_{31}, \phi\right\}\middle| E_{\alpha\beta}^{\mathrm{amp}}(t) \leqslant E_{\alpha\beta}^{0}, 0 \leqslant t \leqslant T\right\}, \tag{12}$$

which form the control function space in Fig. 1(b). In addition, we note that although $\phi_{\alpha\beta}$ can be time dependent by implementing chirps in a microwave generator, the relative phase ϕ is usually assumed to be time independent [18–37,41–56]. For simplicity, we have assumed that all the phases $\phi_{\alpha\beta}$ are time independent, such that they can be absorbed in the definitions of the working states, yielding $\{\Omega_{12}(t), \Omega_{23}(t)\} \geqslant 0$ and $\Omega_{13} = |\Omega_{13}(t)|e^{i\phi}$.

Secondly, we build the time-dependent control parameters by the Fourier decomposition as

$$E_{\alpha\beta}^{\mathrm{amp}}(t) = \left|\sum_{m=0}^{N}[A_{\alpha\beta,m}\cos(\omega_m t) + B_{\alpha\beta,m}\sin(\omega_m t)]\right| \tag{13}$$

with $\omega_m = mv_{\max}/N$. Then, our task is transferred to a multiparameter optimization problem of $\mathcal{L}$. We solve it using the built-in algorithms in MATLAB's Optimization Toolbox. With the output $\{A_{\alpha\beta,m}, B_{\alpha\beta,m}, \Delta_{21}, \Delta_{31}, \phi\}$, we can obtain the QOC protocols of ESST with the help of Eq. (13).

III. TIGHTNESS OF LOWER BOUND FOR ESST

A. QOC protocol for 1,2-propanediol

In this section, we will turn to the key issue of our interest, i.e., whether the bound analytically obtained in Eq. (11) is tight. For this purpose, we first apply the developed QOC approach to a specific chiral molecule at a fixed operation time. Specifically, we use 1,2-propanediol as an example in our discussions, which is a typical chiral molecule studied in cold gaseous experiments [24,25,34]. The working states are three rotational states $|1\rangle_Q = |0,0,0\rangle_Q$, $|2\rangle_Q = |1,-1,0\rangle_Q$, and $|3\rangle_Q = (|1,1,1\rangle_Q + |1,1,-1\rangle_Q)/\sqrt{2}$ in the $|J,\tau,M\rangle$ notation [72]. They are selected by the frequencies and the

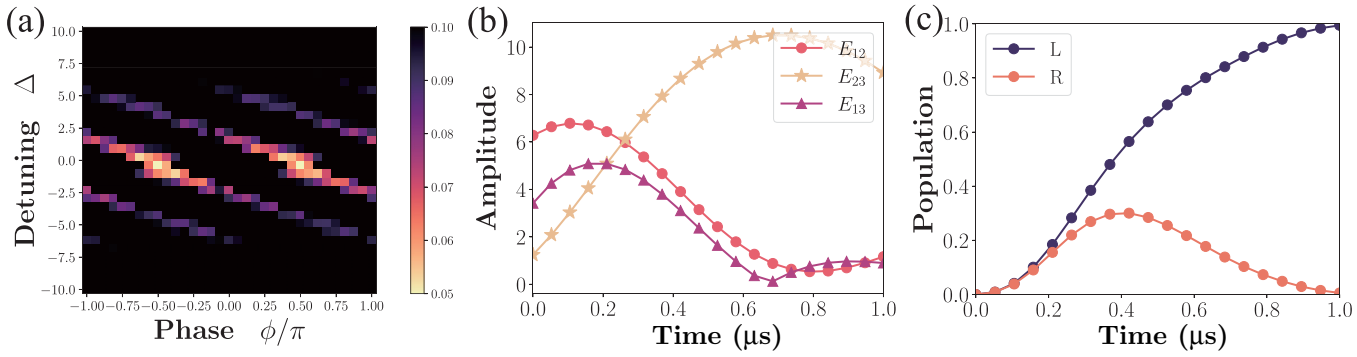

FIG. 2. (a)–(c) QOC protocol for 1,2-propanediol at $T = 1\,\mu s$. (a) shows $\mathcal{L}$ as a function of the detuning ($\Delta_{21} = \Delta_{31} = \Delta$) and the phase ϕ. For convenience, we have normalized $\mathcal{L}$ by the maximum value in the plane. The QOC protocol is obtained at $\Delta = 0$ and $\phi = \pm\pi/2$, whose pulse shapes are given in (b) in the unit of MHz/Debye $\simeq 0.32\,V/cm$. (c) gives the corresponding evolutions of populations for the left- and right-handed molecules. For the QOC protocol, $\eta \simeq 99.5\% \to 1$, and thus the bound in Eq. (11) is tight. (c) gives the corresponding evolutions of populations for the left- and right-handed molecules.

polarizations of the driving fields [72]. The transition electric dipoles (in the unit of Debye) are $|\mu_{12}| = 0.693$, $|\mu_{23}| = 0.958$, and $|\mu_{13}| = 0.211$ [72]. We set $T = 1\,\mu s$ and $E^0_{\alpha\beta} = \Omega_0/|\mu_{\alpha\beta}|$ with $\Omega_0 = 20$ MHz. Other parameters for calculations are $v_{max} = 1$ MHz, $N = 30$, $\zeta = w/(1+w)$, and $\xi = 1/(1+w)$ with $w = 125$. Tolerance for optimization is $\tilde{\epsilon} = 10^{-6}$. For more discussions on the choice of v_{max}, w, N, and $\tilde{\epsilon}$, see Appendix B 1

Firstly, we explore the effect of the detunings and the relative phase on optimizing the conjoint cost. To this end, we fix them and numerically optimize $\mathcal{L}$ with respect to $\{A_{\alpha\beta,m}, B_{\alpha\beta,m}\}$. For simplicity, we set $\Delta_{21} = \Delta_{31} \equiv \Delta$. The results of the optimized $\mathcal{L}$ are given in Fig. 2(a), where 32×32 cases are numerically addressed. Our results indicate that $\Delta = 0$ and $\phi = \pm\pi/2$ are energy-cost favored over other options. Our optimized phase relationships align with the analytical values, highlighting the significance of specific phase relationships in achieving optimal ESST.

In Fig. 2(b), we give the pulse shapes to optimize $\mathcal{L}$ in the case $\Delta = 0$ and $\phi = \pm\pi/2$, which are obtained by inserting the corresponding $\{A_{\alpha\beta,m}, B_{\alpha\beta,m}\}$ in Table I in Appendix B 1 into Eq. (13). Figure 2(c) gives the evolutions of the populations in $|3\rangle_Q$ for the optimal control protocol corresponding to Fig. 2(b). Because two enantiomers are initially in their ground state, at the very beginning of the control, the populations in the state $|3\rangle$ increase for the two enantiomers. After $4\,\mu s$, the population of one enantiomer in the state $|3\rangle$ still increases, and that of the other enantiomers decreases. We find that the final populations in $|3\rangle_Q$ are $|\langle\psi_f^L|3\rangle|^2 \simeq 99.93\%$ and $|\langle\psi_f^R|3\rangle|^2 \simeq 0.10\%$. The corresponding enantiomeric enrichment is $\epsilon_3 \simeq 99.83\%$, approaching the perfect efficiency. When the overall phase changes from ϕ to $\phi + \pi$, the dynamics of the left- and right-handed molecules under CTL models change to each other [18–20]. For the case of $\phi = -\pi/2$, we will have a near-perfect ESST with $\epsilon_3 \simeq -99.83\%$. We note that it is analytically shown [51] that the minimal overall pulse area for perfect ESST is 2π. In our protocol, there is a small deviation from the perfect ESST, and the overall pulse area is $\Theta_{12} + \Theta_{13} + \Theta_{23} \simeq 1.975\pi$, where $\Theta_{\alpha\beta} \equiv \int_0^T \Omega_{\alpha\beta}(t)dt$ are the pulse areas of the three pulses.

B. Time-scaling property for QOC protocols

Before going further, we would like to provide an important property of QOC. As we have shown, the QOC protocols are obtained at $\Delta_{12} = \Delta_{13} = 0$, i.e., the one-photon resonance condition. Under the one-photon condition, the Schrödinger equation of the two enantiomers can be expressed in a time-scaled way as

$$i\hbar\partial_\tau|\psi^{L/R}(\tau)\rangle = \sum_{\alpha>\beta=1}^{3}[\tilde{\Omega}_{\alpha\beta}(\tau)|\alpha\rangle\langle\beta| + \text{H.c.}]|\psi^{L/R}(\tau)\rangle. \quad (14)$$

with $\tau = \lambda t$ and $\tilde{\Omega}_{\alpha\beta}(\tau) = \Omega_{\alpha\beta}(\lambda t)/\lambda$. Then, if the controls at time T can obtain the ultimate limit of $\epsilon_\alpha = 1$, the scaled controls with

$$T \to \lambda T,\ \Omega_{\alpha\beta}(t) \to \Omega_{\alpha\beta}(\lambda t)/\lambda \quad (15)$$

will also give $\epsilon_\alpha = 1$ at λT. On the other hand, the energy cost is scaled as

$$\mathcal{E}_{\text{total}}(T) \to \lambda^{-1}\mathcal{E}_{\text{total}}(T), \quad (16)$$

which is given by inserting the scaling rule in the definition of the energy cost $\mathcal{E}_{\text{total}}(T) \equiv \sum_{\alpha>\beta=1}^{3}\int_0^T |E_{\alpha\beta}(t)|^2 dt$. Because of Eq. (16), we can conclude that if a control is the optimized control at T, its scaled control according to Eq. (15) is the optimized control at other operation times. This property is named the time-scaling property for QOC protocols. As we will show, this property is important to verify the tightness of the bound Eq. (11).

C. Tightness of the bound for 1,2-propanediol

With the QOC protocols at hand, we can numerically confirm the tightness of our bound in Eq. (11). To this end, we define

$$\eta \equiv \frac{\mathcal{L}_{\text{Geo}}}{\mathcal{L}}. \quad (17)$$

By inserting the pulse shapes of Fig. 2(b) into Eq. (4), we obtain the energy cost of the control protocols $\mathcal{E}^{\text{"Q"}}_{\text{total},3}$. Combining this with the obtained efficiency ε_3, we obtain the conjoint

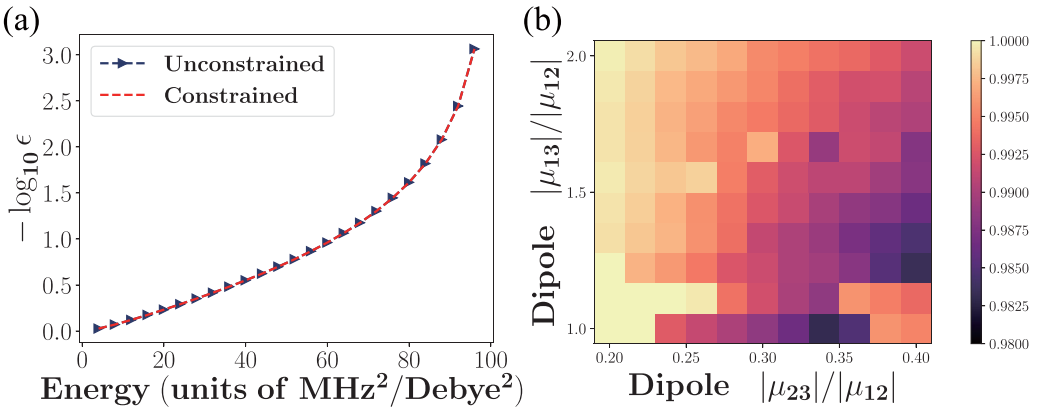

FIG. 3. (a) The corresponding minimal $\epsilon = 1 - |\epsilon_3|$ for different energy input of the pulses. The "unconstrained" and "constrained" denote the results given by optimizing the pulse of the form Eqs. (13) and (18), respectively. (b) $\eta(\to 1)$ in the $|\mu_{13}|/|\mu_{12}| - |\mu_{23}|/|\mu_{12}|$ plane at $T = 1$ μs, suggesting the bound is tight for other chiral molecules.

cost of our protocols $\mathcal{L}$. Further, we insert the pulse shapes of Fig. 2(b) and the efficiency ε_3 into Eq. (7) to obtain $\mathscr{L}_{\text{Geo}}$, yielding $\mathcal{L}_{\text{Geo}} \equiv \mathscr{L}^2_{\text{Geo}}/T$. For the QOC protocol with pulse shapes in Fig. 2(b), we have $\eta \simeq 99.5\%$, approaching the maximum value $\eta = 1$. Thus, at $T = 1$ μs, the obtained QOC protocol works on the boundary of Eq. (11).

As we can see in Eq. (11), the bound should be tight at different operation times. To answer this question, we turn to the obtained scaling property. The scaling property tells whether a control is the optimized control at T, its scaled control according to Eq. (15) is the optimized control at other operation times λT. Then, according to Eq. (16), the conjoint cost of the QOC protocol at λT is given as $\mathcal{L}(\lambda T) = \lambda^{-1}\mathcal{L}(T)$ by taking $\epsilon \simeq 0$, while $\mathscr{L}^2_{\text{Geo}}$ remains unchanged under this transformation. Then, we conclude that the bound is tight, i.e., $\mathcal{L}T/\mathscr{L}^2_{\text{Geo}} = 1$ at different operation times.

To further confirm the tightness of the bound, we turn to the equality condition of the Cauchy-Schwarz inequality. The equality condition indicates that the optimal protocol lying on the boundary should keep the total energy input constant over time. Here, we can take the spherical coordinates to make $\mathscr{E}_{\text{total}}(T)$ constant:

$$
\begin{aligned}
E^{\text{amp}}_{12}(t) &= \sqrt{\frac{\mathscr{E}_{\text{total}}(T)}{T}}|\sin(\vartheta(t))\cos(\varphi(t))|,\\
E^{\text{amp}}_{13}(t) &= \sqrt{\frac{\mathscr{E}_{\text{total}}(T)}{T}}|\sin(\vartheta(t))\sin(\varphi(t))|,\\
E^{\text{amp}}_{23}(t) &= \sqrt{\frac{\mathscr{E}_{\text{total}}(T)}{T}}|\cos(\vartheta(t))|,
\end{aligned}
\tag{18}
$$

which satisfies $\frac{1}{2}\sum_{\alpha,\beta}|E^{\text{amp}}_{\alpha\beta}(t)|^2 = \mathscr{E}_{\text{total}}(T)/T$ so that $\eta = 1$. For simulation, we use the differential form of $\vartheta(t)$ and $\varphi(t)$ to express the protocol. Specifically, we divide $[0, T]$ into $N-1$ discrete equidistant intervals $[t_k, t_{k+1}]$, $k = 0, \ldots, n$ with $t_k = k\Delta t$. $\vartheta(t)$ and $\varphi(t)$ become constant ϑ_k, φ_k within $[t_k, t_{k+1}]$. The pulse is completely determined by the corresponding φ_k and ϑ_k. Accordingly, the protocol $E^{\text{amp}}_{\alpha\beta}(t)$ turns into $E^{\text{amp}}_{\alpha\beta}(k)$ by replacing the $\vartheta(t)$ and $\varphi(t)$ with ϑ_k and φ_k.

Utilizing Eq. (18), we can further explore the maximal ϵ_3 while the energy input is constrained. We note that the input energy can be determined as an initial parameter via the form of Eq. (18). That means we can fix the energy, and turn to the search the maximum efficiency. To this, we optimize the cost functional of efficiency $\mathcal{L}_{\text{target}} = 1 - |\epsilon_3|$ directly with a determined input energy and obtain the minimal $|\epsilon_3|$ for every input energy, which is shown as the red dotted line shown in Fig. 3(a). Here, we show the example of 1,2-propanediol within operation time $T = 1$ μs with detuning $\Delta = 0$ and $\phi = \pi/2$. The temporal difference is $\Delta t = t_{k+1} - t_k = 1/40T$, for $k = 1, \ldots, N$. The tolerance for optimization is $\tilde{\epsilon} = 10^{-6}$.

On the other hand, we can also use the method mentioned in Eq. (13) to give the relationship between minimal energy and efficiency. That is, we can determine the target efficiency and research for the minimal energy. By using the common pulse form Eq. (13) and optimizing the functional $\mathcal{L}_{\text{target}} = \zeta(|\varepsilon_3 - \epsilon_{\text{target}}|)T + \xi\mathscr{E}_{\text{total}}$, we can obtain the optimized energy for a given ϵ_{target}. Then, we traversal every $\epsilon_{\text{target}} \in [0, 1]$ as the initial parameter and obtain the corresponding minimal energy, which is shown as the blue dotted line in Fig. 3(a). Other parameters for calculations are $v_{\max} = 1$ MHz, $N = 30$, $\zeta = w/(1+w)$, $\tilde{\epsilon} = 10^{-6}$, detuning $\Delta = 0$, $\phi = \pi/2$, and $\xi = 1/(1+w)$ with $w = 125$.

The two well-matched curves indicate that the optimal pulses we obtained previously are indeed very close to the optimal solution, while confirming that the equality condition is strictly satisfied. These two curves reveal a trade-off relation between $\mathscr{E}_{\text{total}}(T)$ and ϵ. Generally speaking, a lower ϵ leads to higher energy input accordingly. Beyond this, we also developed an improved approach to find the optimal ESST [i.e., Eq. (18)]. Compared with the standard approach [i.e., Eq. (13)], it reduced the parameters by one-third.

D. Universality of tight bound

Besides the particular example of 1,2-propanediol, the bound is tight for other chiral molecules. In our discussions, different molecular species can be distinguished by the ratios between electric transition dipoles. Then, we applied our optimal-control approach to 11×11 cases in the

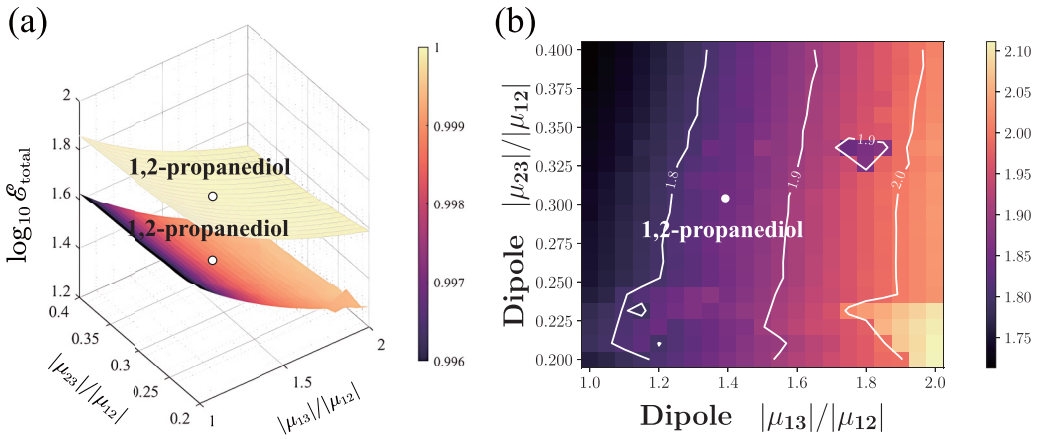

FIG. 4. (a) The energy costs for QOC protocols (lower plane), $\mathscr{E}_{\text{total}}^{\text{"Q"}} = \min_{\alpha=1,2,3}\{\mathscr{E}_{\text{total},\alpha}^{\text{"Q"}}\}$, and the energy costs for the optimized $\pi/2 - \pi - \pi/2$ approach (upper plane), $\mathscr{E}_{\text{total}}^{\text{"}\pi/2\text{"}} = \min_{i=1,2,3}\{\mathscr{E}_{\text{total},s_i}^{\text{"}\pi/2\text{"}}\}$, at $T = 1\,\mu\text{s}$. The colors depict efficiency. (b) Direct comparison between the energy costs, i.e., $\mathscr{E}_{\text{total}}^{\text{"}\pi/2\text{"}}/\mathscr{E}_{\text{total}}^{\text{"Q"}}$.

$|\mu_{13}|/|\mu_{12}| - |\mu_{23}|/|\mu_{12}|$ plane at $T = 1\,\mu\text{s}$. We give η in Fig. 3(b), which is larger than 98%. That is to say, the bound is tight for other chiral molecules in the case of high efficiency. For calculations, we use $|\mu_{12}| = 0.693$ Debye and fix $\Delta = 0$ and $\phi = \pi/2$. The calculations are done following the process used in the example of 1,2-propanediol.

E. Energy-time cost advantage of QOC protocols

To show the advantages of QOC protocols, we compare them with the protocols in the "$\pi/2 - \pi - \pi/2$" approach used in experiments [36,37]. In such an approach, three pulses are applied orderly with no temporal overlaps under $\Delta_{12} = \Delta_{13} = 0$ and $\phi = \pm\pi/2$. The pulse area of the second pulse is π. The pulse areas of the other two are $\pi/2$. Here, we would like to show that the energy cost can be further improved by choosing appropriate pulse shapes with fixed pulse areas. Specifically, we can apply the three pulses in the $E_{12} - E_{23} - E_{13}$ order. The pulse areas are set as $\Theta_{12} = \Theta_{13} = \pi/2$ and $\Theta_{23} = \pi$. Then, the optimal energy cost of $\pi/2 - \pi - \pi/2$ at operation time T is

$$\mathscr{E}_{\text{total},s_1}^{\text{"}\pi/2\text{"}} = \frac{1}{T}\left(\frac{1}{2|\mu_{12}|} + \frac{1}{2|\mu_{13}|} + \frac{1}{|\mu_{23}|}\right)^2 \pi^2, \tag{19}$$

which is obtained when three fields are square pulses with the same amplitude and well-designed pulse lengths as

$$E_{\alpha\beta} = E = \sum_{\alpha>\beta=1}^{3} \frac{\Theta_{\alpha\beta}}{|\mu_{\alpha\beta}|T}, \tau_{\alpha\beta} = \frac{\Theta_{\alpha\beta}}{E|\mu_{\alpha\beta}|}. \tag{20}$$

For the proofs, see Appendix A 2.

In Fig. 4(a), we compare the energy costs between QOC protocols (lower plane) and optimal protocols of the $\pi/2 - \pi - \pi/2$ approach (upper plane) at the operation time of $T = 1\,\mu\text{s}$. To this end, we numerically optimize the three cases of $\epsilon \equiv \sqrt{1 - |\varepsilon_\alpha|}$ with $\alpha = 1, 2, 3$ (for more details, see Appendix B). The minimal energy costs, $\mathscr{E}_{\text{total}}^{\text{"Q"}} = \min_{\alpha=1,2,3}\{\mathscr{E}_{\text{total},\alpha}^{\text{"Q"}}\}$, are given in the lower plane in Fig. 4(a). The minimal energy costs are obtained at $\alpha = 3$. The $\pi/2 - \pi - \pi/2$ method can be further optimized by changing the pulse sequences (see Appendix A 2). The minimal energy costs, $\mathscr{E}_{\text{total}}^{\text{"}\pi/2\text{"}} = \min_{i=1,2,3}\{\mathscr{E}_{\text{total},s_i}^{\text{"}\pi/2\text{"}}\}$, are given in the upper plane in Fig. 4(a). The colors of the planes show their corresponding efficiencies. To give a direct comparison, we give $\mathscr{E}_{\text{total}}^{\text{"}\pi/2\text{"}}/\mathscr{E}_{\text{total}}^{\text{"Q"}}$ in Fig. 4(b), which clearly shows that our optimal control protocols are approximately two times more energy efficient than the $\pi/2 - \pi - \pi/2$ method.

IV. THE EFFECT OF THE REAL FACTORS

In this section, we turn to discuss our QOC protocols in two typical experimental environments for ESST: the cold molecular beams [35–37] and buffer-gas cells [34]. In the cold molecular beams [37], the experimental conditions are close to the ideal conditions adopted in our calculations. More specifically, we would like to compare the control parameters to the experimental parameters.

A. Doppler effect

The Doppler full width at half maximum is calculated as [73]

$$\Delta\nu_{ij} = \omega_{ij}\sqrt{\frac{8k_B T \ln 2}{mC^2}}, i, j = 1, 2, 3, i \neq j, \tag{21}$$

where ω_{ij} is the difference between the level i and j, and k_B is the Boltzmann constant. T and m are the temperature and mass of 1,2-propanediol, respectively. C is the velocity of light in the vacuum. For the state $|1\rangle = |0, 0, 0\rangle$, $|2\rangle = |1, -1, 0\rangle$, $|3\rangle = (|1, 1, 1\rangle + |1, 1, -1\rangle)/\sqrt{2}$, we have

$$\begin{aligned}
&\omega_{12} = 2\pi \times 5781.09\,\text{MHz}, \Delta\nu_{12} = 2\pi \times 1.5 \times 10^{-3}\,\text{MHz},\\
&\omega_{13} = 2\pi \times 12212.15\,\text{MHz}, \Delta\nu_{13} = 2\pi \times 3.2 \times 10^{-3}\,\text{MHz},\\
&\omega_{23} = 2\pi \times 6431.06\,\text{MHz}, \Delta\nu_{23} = 2\pi \times 1.7 \times 10^{-3}\,\text{MHz}.
\end{aligned} \tag{22}$$

Here, we choose $m = 1.264 \times 10^{-25}$ kg and typical temperatures are about $1 \sim 10$ K [34–37]. We have the order $\Delta\nu_{ij} \approx 10^{-2}$ MHz, which is much less than the coupling strength

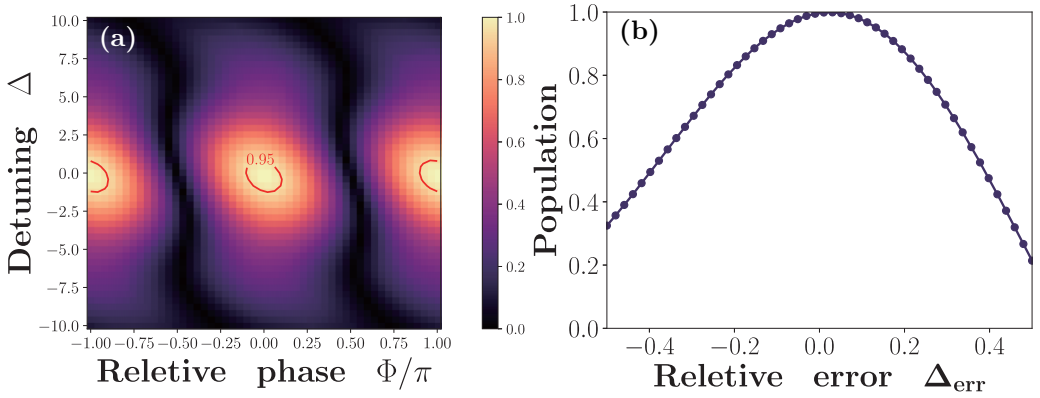

FIG. 5. Robustness against system errors. (a) The resulted $|\varepsilon_3|$ on the $\Delta - \Phi$ plane at $\Delta_{\rm err} = 0$. (b) The resulted $|\varepsilon_3|$ with the variation of $\Delta_{\rm err}$ at $\Delta = 0$ and $\Phi = 0$.

$\Omega_{ij} \approx 10$ MHz. Thus, the effect of the Doppler shift can be negligible in our discussions.

B. The effect of the system errors

We also discuss the robustness of QOC protocols for 1,2-propanediol at $T = 1\,\mu$s. We are interested in the coupling strengths, the detuning, and the overall phase. For the coupling strengths, we have

$$\Omega_{{\rm sim},\alpha\beta}(t) = \Omega_{\alpha\beta}(t)(1 + \Delta_{\rm err}), \tag{23}$$

where $\Omega_{\rm sim}(t)$ deviate from the designed values $\Omega_{\alpha\beta}(t)$ and the related error is given as $\Delta_{\rm err}$. For the detuning, we have

$$\Delta_{12} = \Delta_{13} = \Delta, \tag{24}$$

where the designed value is $\Delta = 0$. For the overall phase, we have

$$\phi = \pi/2 + \Phi, \tag{25}$$

where ϕ deviates from the designed value of $\pi/2$ by Φ. The numerical results are given in Fig. 5. Figure 5(a) shows the resulted $|\varepsilon_3|$ on the $\Delta - \Phi$ plane at $\Delta_{\rm err} = 0$. Figure 5(b) shows the resulted $|\varepsilon_3|$ with the variation of $\Delta_{\rm err}$ at $\Delta = 0$ and $\Phi = 0$. We find that the system errors of Δ and ϕ should be restricted in ± 2.52 MHz and $\pm 0.105\pi$ to provide the highly efficient ESST with $|\varepsilon_3| \geqslant 95\%$. To obtain the same efficiencies, the relative system errors of $\Omega_{\alpha\beta}$ should be restricted in $[-9.7\%, 12.3\%]$. These results show that QOC protocols are robust against system errors.

C. Decoherence

For the decoherence in the molecular beams, the decoherence is negligible in the time scale with $T \leqslant 6\,\mu$s [36]. This is the case in our calculations. Here, we would like to give the master equation to describe the effect of collisions on rotational transitions. We assume the probability of a collision in the time interval dt is Γdt. For convenience, we assume that the branch ratios of all the collision channels are equal, i.e., Γdt. After the collision, the density matrix should become the thermal state $\rho(t + dt) = \rho_{\rm th}$. The probability of no collision in the time region between t and $t + dt$ is $1 - \Gamma dt$. In this case, the final state at $t + dt$ is $\rho(t + dt) = \rho(t) - {\rm i}[{\rm H}, \rho]{\rm dt}$. We can explicitly combine these two probabilities and the dynamics can be written as $\rho(t + dt) = (1 - \Gamma dt)\{\rho(t) - {\rm i}[{\rm H}, \rho]{\rm dt}\} + \rho_{\rm th}\Gamma{\rm dt}$. By ignoring the second-order quantity $O(dt^2)$, we obtain

$$\frac{\partial \rho}{\partial t} = -{\rm i}[{\rm H}, \rho] - \Gamma(\rho - \rho_{\rm th}). \tag{26}$$

The spontaneous emission for rotational transitions is of the order of 10^{-10} Hz (see Ref. [16] for detailed calculations). Then, at a time scale of $\sim 1\,\mu$s, the spontaneous emissions of chiral molecules in the buffer gaseous cells are neglected in our discussions.

As it said in Ref. [34], "Molecules collide with helium atoms approximately every $\tau_c \simeq 6\,\mu$s". Then, we have $\Gamma \simeq 1/6$ MHz. We focus on the Hilbert space of the three working states for simplicity. For calculations, we have set $\rho_{\rm th} = 0.3349|1\rangle\langle 1| + 0.3334|2\rangle\langle 2| + 0.3317|3\rangle\langle 3|$, which corresponds to the thermal state at $\mathcal{T} = 10$ K. The energies of the working states are $\omega_1 = 0$, $\omega_2 = 2\pi \times 5781.09$ MHz, $\omega_3 = 2\pi \times 12212.15$ MHz. As we have explained, the perfect initial state is available in experiments. Therefore, the initial states for calculations are given as $|1\rangle_L$ and $|1\rangle_R$ for the two enantiomers. In Fig. 6(a), we show the pulse shapes of the optimal control at 1 μs. The other parameters are $\Delta_{21} = \Delta_{31} = 0$ and $\phi = \pi/2$. The constraint on the strengths of the pulses as $E_{\alpha\beta} \leqslant E^0_{\alpha\beta} \simeq 3.2$ V/cm. The evolutions of the populations in the states $|3\rangle_Q$ are given in Fig. 6(b). The final populations in the states $|3\rangle_Q$ are about 89.69% and 5.19%. The resulting efficiency under the decoherence is about 84.50%. Beyond this, we also give the pulse shapes [Fig. 6(c)] and the evolution of the populations in the state $|3\rangle_Q$ [Fig. 6(d)] under the constraint of $E_{\alpha\beta} \leqslant E^0_{\alpha\beta} \simeq 0.4$ V/cm. The final populations are 50.81% and 24.49%. The efficiency is 26.32%. The effect of decoherence can be modeled as

$$\varepsilon_3^{dc} \simeq \varepsilon_3 \exp\left(-\frac{T}{\tau_c}\right), \tag{27}$$

where ε_3 is the predicted efficiency in the absence of decoherence, T is the operation time, and τ_c is the decoherence time. To see this clearly, we show the numerical results by solving the master equations in Fig. 6(e). The function of Eq. (27) is given in Fig. 6(e) for comparison. We can see that they agree with each other well. For different operation times, the pulse

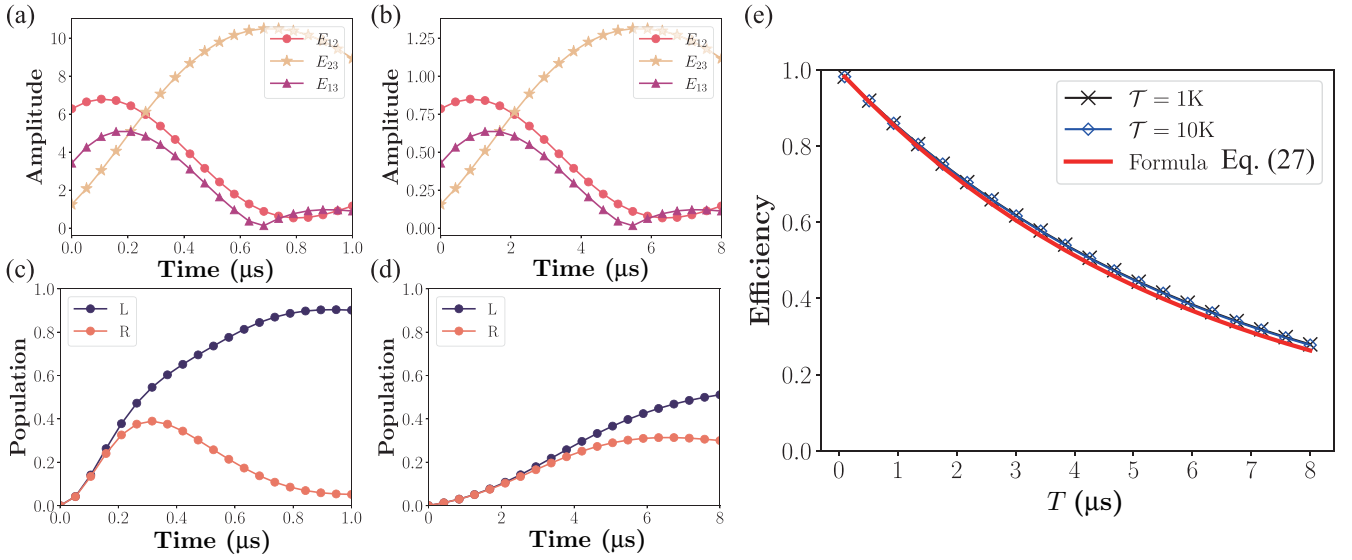

FIG. 6. Effect of decoherence on our protocols in the buffer gas cell. (a) and (b) Pulse shapes at $T = 1\,\mu$s and the corresponding evolutions of populations in the states $|3\rangle_Q$. The unit is MHz/Debye $\simeq 0.32$ V/cm. The constraint on the strengths of the pulses as $E_{\alpha\beta} \leqslant E^0_{\alpha\beta} \simeq 3.2$ V/cm. (c) and (d) The corresponding results at $T = 8\,\mu$s. The constraint on the strengths of the pulses as $E_{\alpha\beta} \leqslant E^0_{\alpha\beta} \simeq 0.4$ V/cm, which corresponds to the experimental used values in Ref. [34]. (e) The efficiencies as a function of T for our optimal controls. The numerical results agree well with Eq. (27). For different operation times, the pulse shapes are given by applying the scaling rules $T \to \lambda T$ and $E_{\alpha\beta}(t) \to E_{\alpha\beta}(\lambda t)/\lambda$ to the case of $T = 1\,\mu$s. The master equations are solved at $\Gamma = 1/6$ MHz and $\rho_{\rm th} = 0.3349|1\rangle\langle 1| + 0.3334|2\rangle\langle 2| + 0.3317|3\rangle\langle 3|$ with $\mathcal{T} = 10$ K.

shapes are given by applying the scaling rules $T \to \lambda T$ and $E_{\alpha\beta}(t) \to E_{\alpha\beta}(\lambda t)/\lambda$ to the case of $T = 1\,\mu$s.

D. Initial state and others

In our discussions, we have assumed the initial ground state of the two enantiomers. The perfect single initial state can be prepared by using UV lasers to selectively deplete the populations of the excited states in the CTL models [36,37] or using a CTL model with two excited states in higher vibrational levels [74]. When the molecules are initially in thermal states and the working states are in the vibrational ground state, all three working states are occupied. Then, the perfect ESST is impossible for the decoherence-free case where the dynamics of the molecules are described by unitary transformations. For the couplings to the states outside the working model, their effects are negligible due to the appropriate design of the driving fields [72] and the well-separated rotational spectra of 1,2-propanediol.

V. CONCLUSION AND OUTLOOK

We have established a geometric frame to discuss the energy-time costs of ESST. We have proven that the curve length linked to vector evolution sets a tight lower bound on the conjoint cost, establishing a benchmark for assessing and refining ESST techniques. We have also provided a quantum optimal control approach to design the ESST control protocols with optimized energy-time cost. The delivered protocols can be directly used in the molecular beams, where the ideal conditions are approximately obtained [37].

Our geometric approach can be extended to the cases of multiple-loop CTL models [52,56] as well as other routes for ESST [1–3]. While robustness against errors was another practical issue in ESST [43,49,55], it is attractive to explore the universal robust quantum control [75] of ESST with optimized energy-time costs. To address the complexity of these issues, we are pleased to see the application of physics-informed neural networks for quantum control [76]. In addition, our optimal control protocols are provided numerically. It is interesting to provide an analytical approach to find the optimal control protocols, which will give a more profound understanding of ESSTs [51]. Beyond these, it is also interesting to study the minimum energy-time costs of ESST from the fundamental quantum mechanics rules [64–67].

ACKNOWLEDGMENTS

We thank Prof. C.-C. Shu for the fruitful discussions on the pulse-area theorem and optimal phase relationships of perfect ESST. Financial support by Quantum Science and Technology-National Science and Technology Major Project (Grant No. 2023ZD0300700), the Science Challenge Project (Grant No. TZ2025017), and the National Natural Science Foundation of China (Grants No. 12088101, No. 12105011, and No. U2330401) is gratefully acknowledged.

APPENDIX A: GEOMETRY APPROACH FOR OPTIMAL ESST

1. General scheme of the bound

The vectors are defined as

$$|\lambda(t)\rangle\!\rangle \equiv \int_0^t [\epsilon, E_{12}(t'), E_{13}(t'), E_{23}(t')]^{\rm T} dt' \tag{A1}$$

with $\epsilon \equiv \sqrt{1-|\varepsilon_3|}$, which form the parameter space. In this space, we define the inner product as

$$\langle\langle \lambda, \lambda \rangle\rangle \equiv \sum_{\mu,\nu=1}^{4} g_{\mu\nu}(\lambda_\mu)^* \lambda_\nu, \tag{A2}$$

where the metric $g_{\mu\nu} = \mathrm{diag}(\zeta, \xi, \xi, \xi)$ with $\{\zeta, \xi\} > 0$ and λ_ν is the νth component of the vector $|\lambda\rangle\rangle$. We note the inner products with properties of positive definiteness, conjugate symmetry, and linearity. The positive definiteness means

$$\langle\langle \lambda, \lambda \rangle\rangle \geqslant 0. \tag{A3}$$

To prove this, we insert Eq. (A1) into Eq. (A2), yielding

$$\begin{aligned}\langle\langle \lambda, \lambda \rangle\rangle =& \zeta \left(\int_0^t \epsilon dt'\right)\left(\int_0^t \epsilon dt'\right)^* \\ &+ \xi \sum_{\alpha>\beta=1}^{3} \left(\int_0^t E_{\alpha\beta} dt'\right)\left(\int_0^t E_{\alpha\beta} dt'\right)^*.\end{aligned} \tag{A4}$$

Because $\{\zeta, \xi\} > 0$, we have $\langle\langle \lambda, \lambda \rangle\rangle \geqslant 0$. The conjugate symmetry is reflected as

$$\langle\langle \lambda_2, \lambda_1 \rangle\rangle = \langle\langle \lambda_1, \lambda_2 \rangle\rangle^*. \tag{A5}$$

Because $E_{\alpha\beta}$ can be complex, we have $\langle\langle \lambda_2, \lambda_1 \rangle\rangle = \langle\langle \lambda_1, \lambda_2 \rangle\rangle^*$. The linearity property is reflected as

$$\langle \lambda_1, a\lambda_2 + b\lambda_3 \rangle = a\langle \lambda_1, \lambda_2 \rangle + b\langle \lambda_1, \lambda_3 \rangle. \tag{A6}$$

To prove this, we give

$$\langle \lambda_1, a\lambda_2 + b\lambda_3 \rangle = \sum_{\mu\nu} g_{\mu\nu}(a\lambda_{\mu 2} + b\lambda_{\mu 3})^* \lambda_{\nu 1} \tag{A7}$$

$$= a\langle \lambda_1, \lambda_2 \rangle + b\langle \lambda_1, \lambda_3 \rangle. \tag{A8}$$

With these properties, we note that the parameter space is a Riemannian manifold.

2. Application in $\pi/2 - \pi - \pi/2$ method

The upper process can be introduced to the $\pi/2 - \pi - \pi/2$ method. To this end, we introduce

$$f(t) = \begin{cases} |\Omega_{12}|/|\mu_{12}| & t \in [0, \tau_{12}], \\ |\Omega_{23}|/|\mu_{23}| & t \in (\tau_{12}, \tau_{12} + \tau_{23}], \\ |\Omega_{13}|/|\mu_{13}| & t \in (\tau_{12} + \tau_{23}, T], \end{cases} \tag{A9}$$

where $\tau_{\alpha\beta}$ are the corresponding durations of the driving field. Utilizing the Cauchy-Schwarz inequality $(\int_a^b f(x)g(x)dx)^2 \leqslant (\int_a^b f^2(x)dx)(\int_a^b g^2(x)dx)$, we have the inequality

$$T\mathscr{E}_{\mathrm{total}} = \left(\int_0^T 1^2 dt\right)\left(\int_0^T |f(t)|^2 dt\right) \geqslant \left(\int_0^T f(t)dt\right)^2. \tag{A10}$$

On the other hand, we have

$$\int_0^T |\Omega_{\alpha\beta}| dt = \Theta_{\alpha\beta}. \tag{A11}$$

That is to say, we have

$$\int_0^T f(t)dt = \sum_{\alpha>\beta}^{3} \frac{1}{|\mu_{\alpha\beta}|} \int_0^T |\Omega_{\alpha\beta}(t)| dt = \sum_{\alpha>\beta}^{3} \frac{\Theta_{\alpha\beta}}{|\mu_{\alpha\beta}|}. \tag{A12}$$

Finally, the general results are given as

$$T\mathscr{E}_{\mathrm{total}} \geqslant \left(\sum_{\alpha>\beta}^{3} \frac{\Theta_{\alpha\beta}}{|\mu_{\alpha\beta}|}\right)^2. \tag{A13}$$

For the optimized $\pi/2 - \pi - \pi/2$ approach, we have

$$\mathscr{E}_{\mathrm{total}} \geqslant \left(\frac{1}{2|\mu_{12}|} + \frac{1}{2|\mu_{13}|} + \frac{1}{|\mu_{23}|}\right)^2 \frac{\pi^2}{T}. \tag{A14}$$

The condition of equality is $f(t) = \text{constant}$. With Eq. (9), we have

$$f = E_{\alpha\beta} = \frac{1}{T} \sum_{\alpha>\beta} \frac{\Theta_{\alpha\beta}}{|\mu_{\alpha\beta}|}. \tag{A15}$$

With Eq. (A11), we have

$$\tau_{\alpha\beta} E_{\alpha\beta} |\mu_{\alpha\beta}| = \Theta_{\alpha\beta}. \tag{A16}$$

Then, we arrive at

$$E_{\alpha\beta} = \frac{1}{T} \sum_{\alpha>\beta=1}^{3} \frac{\Theta_{\alpha\beta}}{|\mu_{\alpha\beta}|}, \quad \tau_{\alpha\beta} = \frac{\Theta_{\alpha\beta}}{E_{\alpha\beta}|\mu_{\alpha\beta}|}. \tag{A17}$$

APPENDIX B: NUMERICAL OPTIMIZATION OF CONJOINT COST

1. Numerical route for optimization of conjoint cost

To obtain the energy-time optimal ESST, we numerically minimize the conjoint cost

$$\mathcal{L} = \zeta(1 - |\varepsilon_3|)T + \xi \mathscr{E}_{\mathrm{total}}. \tag{B1}$$

This problem can be solved more conveniently by assuming the time cost T is fixed. Then, we rewrite the conjoint cost at the fixed time as

$$\tilde{\mathcal{L}} = \frac{w}{1+w}(1 - |\varepsilon_3|) + \frac{1}{1+w}\mathscr{E}_{\mathrm{total}} \tag{B2}$$

with $w = \zeta T/\xi$. In our discussions, the control is given as

$$\mathbb{F} \equiv \left\{ \{E_{\alpha\beta}(t), \Delta_{21}, \Delta_{31}, \phi\} \mid 0 \leqslant E_{\alpha\beta}(t) \leqslant E^0_{\alpha\beta}, 0 \leqslant t \leqslant T \right\} \tag{B3}$$

with

$$E_{\alpha\beta}(t) = \left| A_{\alpha\beta,0} + \sum_{m=1}^{N} [A_{\alpha\beta,m} \cos(\omega_m t) + B_{\alpha\beta,m} \sin(\omega_m t)] \right|, \quad \omega_m = m\nu_{\max}/N \tag{B4}$$

given in the Fourier decomposition. In the main text, we give a more compact form by choosing $B_{\alpha\beta,0} = 0$, which is

$$E_{\alpha\beta}(t) = \left| \sum_{m=0}^{N} [A_{\alpha\beta,m} \cos(\omega_m t) + B_{\alpha\beta,m} \sin(\omega_m t)] \right|. \tag{B5}$$

TABLE I. The coefficient of the Fourier series.

m	$A_{12,m}$	$A_{13,m}$	$A_{23,m}$	$B_{12,m}$	$B_{13,m}$	$B_{23,m}$
1	−0.6302	− 0.9834	−1.9346	− 1.5332	0.5664	0.9226
2	−1.7326	−0.5244	−0.2210	−0.0788	−0.6552	−1.8982
3	0.3340	0.0324	−0.4976	− 1.5698	0.9948	0.6378
4	−1.5976	−0.9786	−1.7716	0.2460	0.9786	0.8196
5	−1.3742	0.8050	0.0812	− 0.8140	0.2024	−1.9298
6	−1.5170	−0.3012	1.6224	−0.4644	−0.3780	−1.2708
7	1.4132	1.4332	1.2998	1.0612	1.9110	−0.8726
8	−1.3818	−1.5432	1.3036	−0.9516	0.6414	−1.9208
9	−0.7482	1.8892	−1.5004	0.7694	0.4688	1.2496
10	1.4140	− 0.5094	−1.5420	0.3458	1.8764	−0.1756
11	0.6020	1.3298	1.2148	0.7920	−0.0988	0.8490
12	−1.9852	0.3852	1.9290	−1.4666	0.6598	0.5490
13	1.0230	1.8306	1.6928	− 0.2260	−0.3912	−0.8084
14	−1.5704	−0.8046	−0.8226	−1.7684	−0.1850	0.3416
15	−0.2342	0.7742	−0.4242	1.0954	0.0744	−1.3376

Then, our task is transferred to finding the parameter set of $\{A_{\alpha\beta,m}, B_{\alpha\beta,m}, \Delta_{21}, \Delta_{31}, \phi\}$ to minimize the functional $\mathcal{L}[\mathbb{F}]$. To this end, we use the built-in optimization algorithms of the Optimization Toolbox in MATLAB. The dynamics of chiral molecules are solved using the fourth-order Runge-Kutta algorithm.

The parameters $\nu_{\max}$ and N are related to the Fourier decomposition of the control fields. The overall number of parameters to be optimized is

$$N_{\text{total}} = 6N + 3. \tag{B6}$$

The coefficient w can be changed to improve the balance between the energy cost and the efficiency. In the built-in optimization algorithms of the Optimization Toolbox in MATLAB, the function tolerance $\tilde{\epsilon}$ is an important parameter. For the numerical results in the main text, the parameters are chosen as $\nu_{\max} = 1$ MHz, $N_{\text{total}} = 93$, $w = 125$, and $\tilde{\epsilon} = 10^{-6}$. Here,

TABLE II. The energy cost and efficiency of the number of pulses.

N_{total}	9	33	63	93
Energy cost	102.5544	97.0180	96.7908	95.7096
Efficiency	0.0894	0.9990	0.9989	0.9983

we expand the $\Omega_{\alpha\beta}$ as the Fourier series:

$$\Omega_{\alpha\beta} = \left| A_{\alpha\beta,0} + \sum_{m=1}^{N} A_{\alpha\beta,m} \cos\left(\frac{2\pi m}{15} t\right) + B_{\alpha\beta,m} \sin\left(\frac{2\pi m}{15} t\right) \right|. \tag{B7}$$

The constant terms $A_{\alpha\beta,0}$ are $A_{12,0} = 1.5850$, $A_{13} = 0.5822$, and $A_{23} = -1.6720$. The coefficients of the other Fourier series are all displayed in Table I.

2. Convergence of the numerical results

In what follows, we would like to justify our choices on $\nu_{\max} = 1$ MHz, $N_{\text{total}} = 93$, $w = 125$, and $\tilde{\epsilon} = 10^{-6}$.

a. About N_{total}

We select $N_{\text{total}} = 9, 33, 63, 93$ to optimize the ESST. Other parameters are $\nu_{\max} = 1$ MHz and $w = 125$. The results are shown in Table II and Fig. 7. At $N_{\text{total}} = 9$, the efficiency of ESST is low. With the increase of N_{total}, the efficiency increases and approaches 1 at $N_{\text{total}} = 33$, $N_{\text{total}} = 63$, and $N_{\text{total}} = 93$. At the same time, the energy cost decreases. By increasing N_{total}, the numerical results will become closer to the true optimal solution. However, in this case, more computational resources are needed. In this sense, we would like to choose $N_{\text{total}} = 93$, where both the efficiency and the energy cost are good enough.

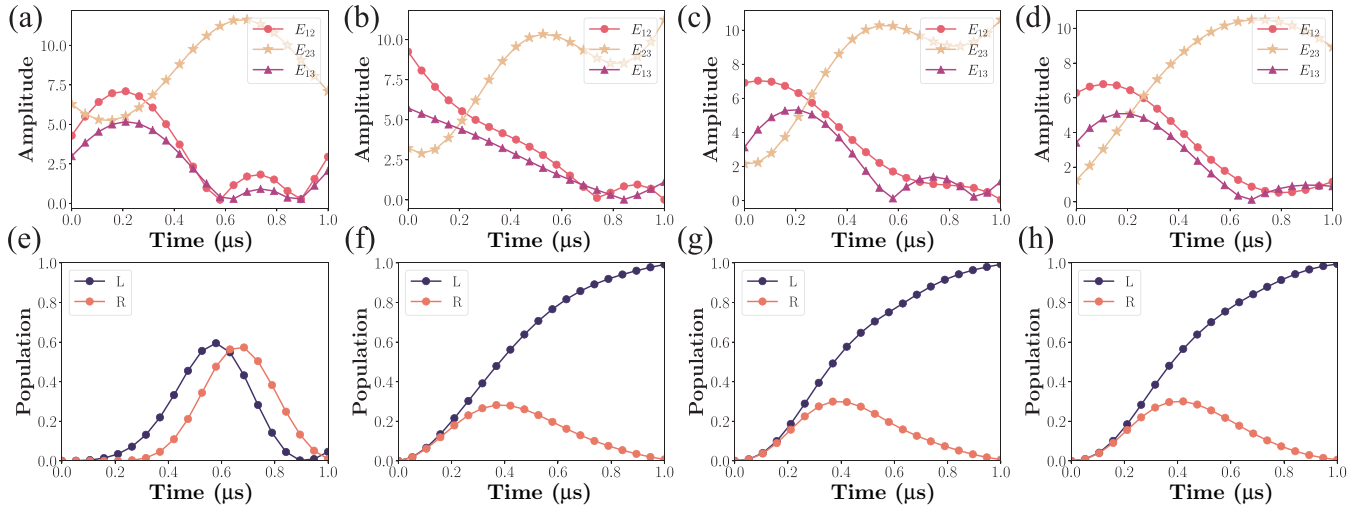

FIG. 7. About N_{total}. The optimized pulses (a)–(c) and the population (d)–(f) for different N_{total}. The corresponding N_{total} are 9 [(a), (e)], 33 [(b), (f)], 63 [(c), (g)], and 93 [(d), (h)].

TABLE III. The energy cost and efficiency of different maximum allowable frequencies.

$\nu_{\max}$	1	5	10	40
Energy cost	95.7096	108.7936	484.2940	1049.9
Efficiency	0.9983	0.9988	0.9982	0.9693

b. About $\nu_{\max}$

We select different maximum allowable frequencies, i.e., $\nu_{\max} = 1$, 5, 10, and 40 MHz, to optimize the ESST. Other parameters are chosen as $N_{\text{total}} = 93$, $w = 125$, and $\tilde{\epsilon} = 10^{-6}$. The results are shown in Table III and Fig. 8. All the results indicate that $\nu_{\max} = 1$ is appropriate.

c. About w

When an excessively large (or small) weight is given, only one target is optimized and the other target is not optimized at all. We select different weights in our calculation, i.e., $w = 12.5$, 25, 125, and 500, to optimize the ESST. The results are shown in Fig. 9 and Table IV. Other parameters are chosen as $\nu_{\max} = 1$ MHz, $N_{\text{total}} = 93$, and $\tilde{\epsilon} = 10^{-6}$. The results for $w = 12.5$ and $w = 500$ show two different extreme conditions. The results of $w = 12.5$ show that only the energy cost is optimized. The results of $w = 125$ show that only the efficiency is optimized. With these results, we selected $w = 125$.

d. About $\tilde{\epsilon}$

The tolerance $\tilde{\epsilon}$ reflects the convergence of the functional. The smaller $\tilde{\epsilon}$, the more accurate optimization is. Here, we select different function tolerance $\tilde{\epsilon}$ in our calculation, i.e., $\tilde{\epsilon} = 10^{-2}$, 10^{-4}, and 10^{-6}, to optimize the ESST. Other parameters are chosen as $\nu_{\max} = 1$ MHz, $N_{\text{total}} = 93$, and $w = 125$. The results are shown in Fig. 10 and Table V. As the function tolerance $\tilde{\epsilon}$ decreases, both the energy cost and the efficiency tend to converge. Thus, considering the computational resources, we choose $\tilde{\epsilon} = 10^{-6}$.

TABLE IV. The energy cost and efficiency of different w.

w	12.5	25	125	500
Energy cost	0.0604	85.3956	95.7096	445.0960
Efficiency	3.4×10^{-5}	0.9748	0.9983	0.9964

APPENDIX C: ABOUT REAL FACTORS

1. Perfect single initial state

In recent experiments [36,37], a UV-depletion technology was developed to ensure the perfect single initial state in the working Hilbert space. They used a continuous-wave UV laser to selectively deplete the population of the target rotational to higher electronic states. After UV excitation, the molecules predominantly radiate back to higher vibrational levels and to other rotational levels in the electric ground state. In this sense, the perfect single initial state is obtained in the working Hilbert space.

To deal with the problem, some of us also proposed the 2IR + MW scheme [74], where the two excited states are in higher vibrational levels and thus are well energetically separated from the ground state. The usually vibrational energy spacings are 100 THz. In this sense, the thermal populations in the two excited states of the CTL model are negligible at $\mathcal{T} = 10$ K.

TABLE V. The energy cost and efficiency of the function tolerance $\tilde{\epsilon}$.

$\tilde{\epsilon}$	10^{-2}	10^{-4}	10^{-6}
Energy cost	119.2616	104.7260	95.7096
Efficiency	0.9991	0.9902	0.9983

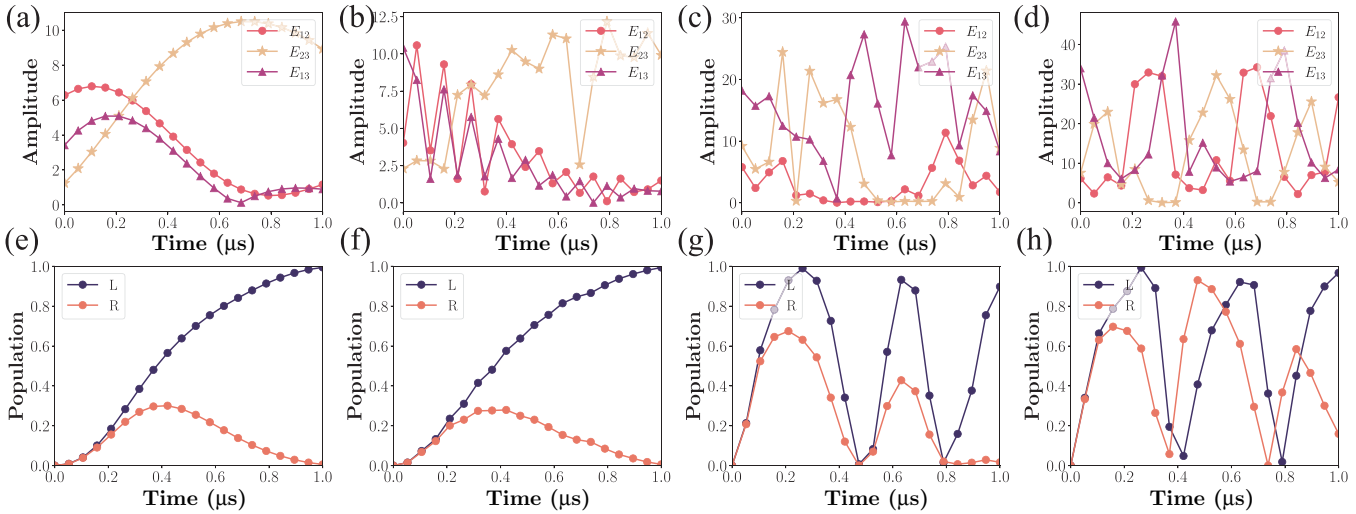

FIG. 8. About $\nu_{\max}$. The optimized pulses (a)–(d) and the population (e)–(h) for different maximum allowable frequencies. The corresponding maximum allowable frequencies (in units of MHz) are 1 [(a), (e)], 5 [(b), (f)], 10 [(c), (g)], and 40 [(d), (h)].

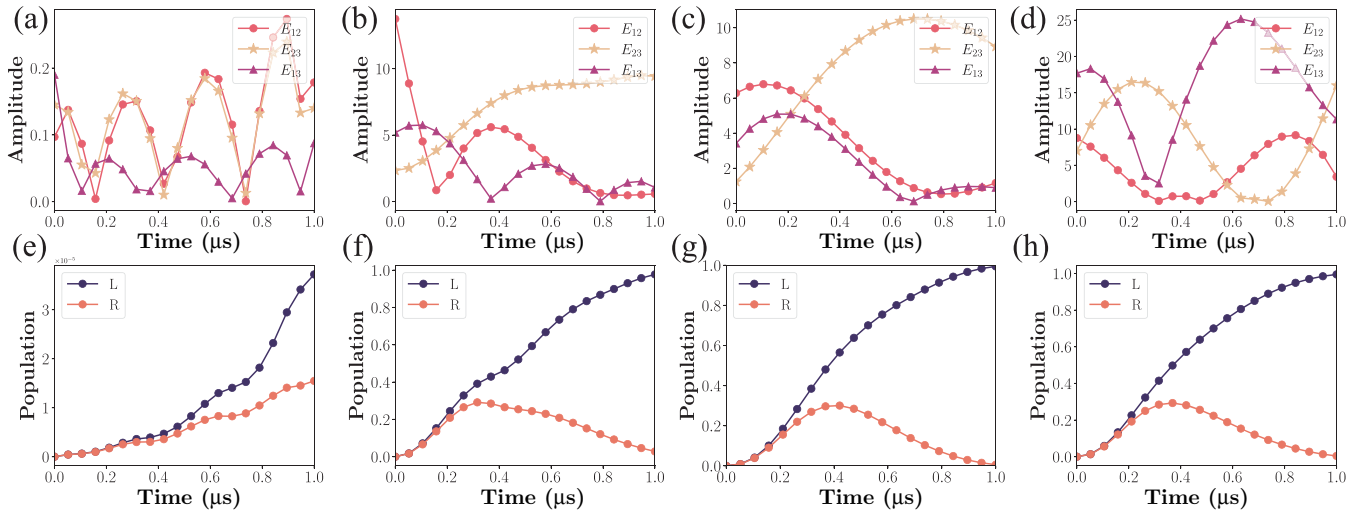

FIG. 9. About w. The optimized pulses (a)–(d) and the population (e)–(h) for different weights w. The weights are 12.5 [(a), (e)], 25 [(b), (f)], 125 [(c), (g)], and 500 [(d), (h)].

2. In what conditions outside couplings are negligible

There are two reasons to assume that the outside couplings are negligible. One is for the appropriate choosing of rotational sublevels of the working state. This is done by choosing appropriate frequencies and the polarizations of the fields. In Ref. [72], some of us explored the rotational selection rules and gave the working model. In this model, the couplings to the states outside the working model that are energy degenerated with the working states are forbidden due to the rotational selection rules. This model was used in recent experiments [36,37].

The other is due to the assumption that the outside couplings are much smaller than the corresponding detunings. The validity of this assumption depends on the molecules and the applied fields. For 1,2-propanediol, the nearest selection-rule-available state has an energy span of $\Delta E \simeq 2\pi \times 849.14 = 5335.3$ MHz from the working model. Then, the coupling strengths can be as large as $\Omega = 0.01\Delta E \simeq 50$ MHz, which is larger than the coupling strengths in our discussions. Therefore, the outside couplings are negligible in our discussions.

Beyond this, it is possible to weaken the effect of the outside couplings by appropriately choosing the working state. In Ref. [56], some of us studied the effect of the nearest outside state (labeled $|4\rangle$) on the cyclic three-level model. Then, the working model became a four-level one with two subloops

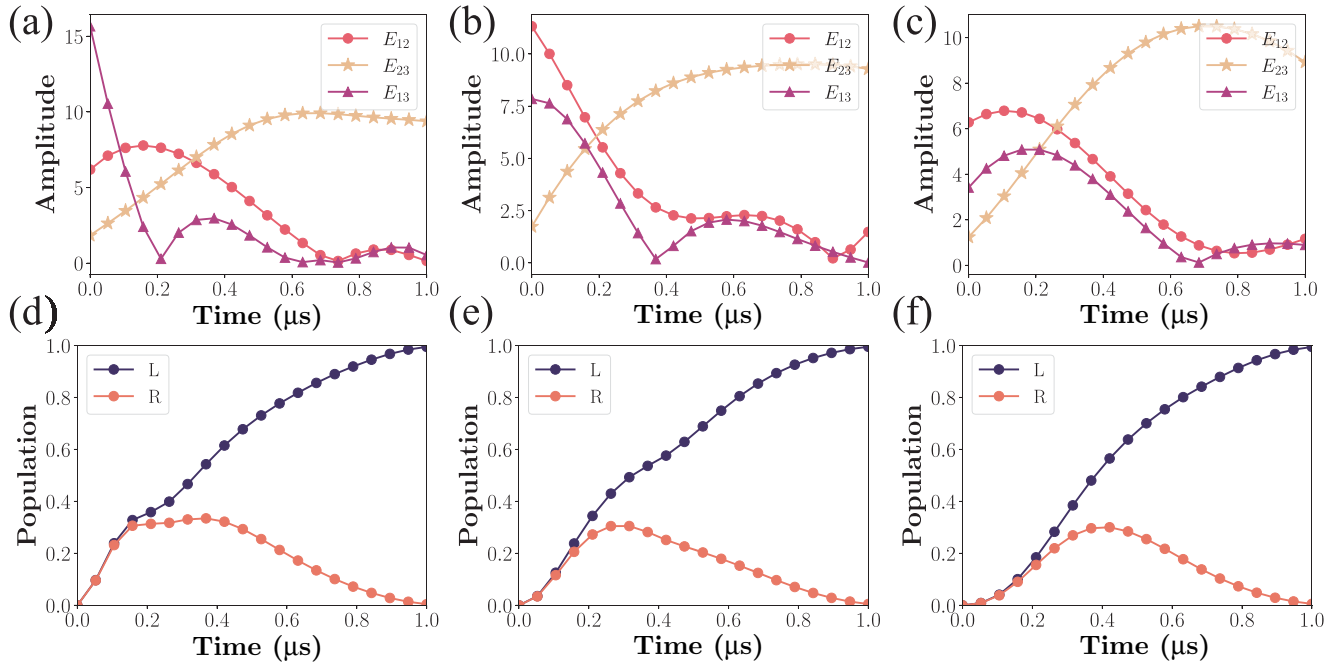

FIG. 10. About $\tilde{\epsilon}$. The optimized pulses (a)–(c) and the population (d)–(f) for different $\tilde{\epsilon}$. The function tolerance are 10^{-2} [(a), (d)], 10^{-4} [(b), (e)], and 10^{-6} [(c), (f)].

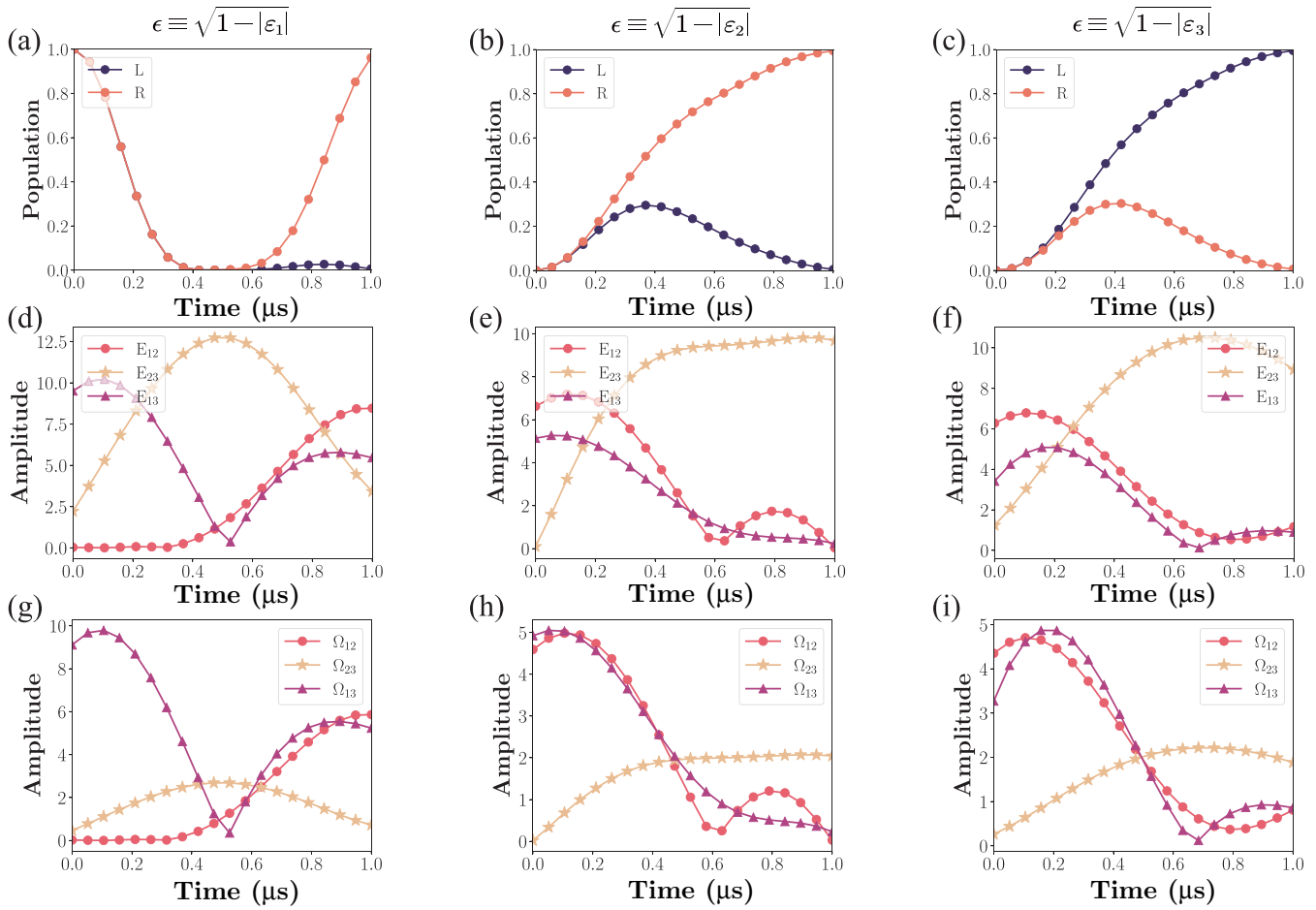

FIG. 11. The optimized results of ESST of 1,2-propanediol for different target states. (a)–(c) give the population evolutions with the target state $|1\rangle$, $|2\rangle$, and $|3\rangle$, respectively. (d)–(f) give the corresponding electric field amplitudes. (g)–(i) give the corresponding Rabi frequencies.

respectively containing $|3\rangle$ and $|4\rangle$. Under $\Delta E \ll \Omega$, the perturbative results in Eq. (13) of Ref. [56] said the ratio between the effect of the two subloops is $\kappa_1\kappa_2$ with $\kappa_1 = \mu_{14}/\mu_{31}$ and $\kappa_2 = \mu_{42}/\mu_{32}$. To weaken the effect of $|4\rangle$, one can appropriately choose the vibrational sublevels of working states to make $\kappa_1\kappa_2 < 1$.

APPENDIX D: QOC PROTOCOLS UNDER DIFFERENT ε_α

In what follows, we give more details on the calculations for the example of 1,2-propanediol, including the pulse shapes, the durations, and Rabi frequencies. Firstly, we set $\epsilon \equiv \sqrt{1-|\varepsilon_1|}$ and apply our numerical optimal approach to obtain the corresponding optimal control protocol. The results are given in Figs. 11(a), 11(d), and 11(g), which give the corresponding evolution of populations in the state $|1\rangle$, the phase shapes, and the Rabi frequencies. We have $\mathscr{E}^{\text{“}Q\text{”}}_{\text{total},1} = 144.8172$. By setting $\epsilon \equiv \sqrt{1-|\varepsilon_2|}$, we give the corresponding results in Figs. 11(b), 11(e), and 11(h). We have $\mathscr{E}^{\text{“}Q\text{”}}_{\text{total},2} = 96.1306$. By setting $\epsilon \equiv \sqrt{1-|\varepsilon_3|}$, we give the corresponding results in Figs. 11(c), 11(f), and 11(i). We have $\mathscr{E}^{\text{“}Q\text{”}}_{\text{total},3} = 95.7096$. By choosing the case with the lowest energy cost $\mathscr{E}^{\text{“}Q\text{”}}_{\text{total}} = 95.7096$, we give the point labeled “1,2-propanediol” in the lower plane in Fig. 3(a) in the main text.

APPENDIX E: OPTIMIZED $\pi/2-\pi-\pi/2$ METHOD UNDER DIFFERENT PULSE SEQUENCES

We can change the pulse sequences to further optimize the $\pi/2-\pi-\pi/2$ method. In the case, E_{12}, E_{23}, and E_{13} are applied orderly. The lowest energy cost is $\mathscr{E}^{\text{“}\pi/2\text{”}}_{\text{total},s_1} = [1/(2|\mu_{12}|)+1/(2|\mu_{13}|)+1/|\mu_{23}|]^2\pi^2/T$. In the case, E_{12}, E_{13}, and E_{23} are applied orderly. The lowest energy cost is $\mathscr{E}^{\text{“}\pi/2\text{”}}_{\text{total},s_2} = [1/(2|\mu_{12}|)+1/(2|\mu_{23}|)+1/|\mu_{13}|]^2\pi^2/T$. In the case, E_{13}, E_{12}, and E_{23} are applied orderly. The lowest energy cost is $\mathscr{E}^{\text{“}\pi/2\text{”}}_{\text{total},s_3} = [1/(2|\mu_{13}|)+1/(2|\mu_{23}|)+1/|\mu_{12}|]^2\pi^2/T$. Then, the lowest energy cost with arbitrary pulse sequences is $\mathscr{E}^{\text{“}\pi/2\text{”}}_{\text{total}} = \min(\mathscr{E}^{\text{“}\pi/2\text{”}}_{\text{total},s_1}, \mathscr{E}^{\text{“}\pi/2\text{”}}_{\text{total},s_2}, \mathscr{E}^{\text{“}\pi/2\text{”}}_{\text{total},s_3})$. For 1,2-propanediol, we have $\mathscr{E}^{\text{“}\pi/2\text{”}}_{\text{total},s_1} = 353.2666$, $\mathscr{E}^{\text{“}\pi/2\text{”}}_{\text{total},s_2} = 168.7536$, and $\mathscr{E}^{\text{“}\pi/2\text{”}}_{\text{total},s_3} = 185.4368$. Then, the lowest energy cost with arbitrary pulse sequences is $\mathscr{E}^{\text{“}\pi/2\text{”}}_{\text{total}} = \min(\mathscr{E}^{\text{“}\pi/2\text{”}}_{\text{total},s_1}, \mathscr{E}^{\text{“}\pi/2\text{”}}_{\text{total},s_2}, \mathscr{E}^{\text{“}\pi/2\text{”}}_{\text{total},s_3}) = 168.7536$.

[1] A. Salam and W. Meath, On the control of excited state relative populations of enantiomers using circularly polarized pulses of varying durations, J. Chem. Phys. **106**, 7865 (1997).

[2] A. Salam and W. Meath, On enantiomeric excesses obtained from racemic mixtures by using circularly polarized pulsed lasers of varying durations, Chem. Phys. **228**, 115 (1998).

[3] Y. Ma and A. Salam, On chiral selectivity of enantiomers using a circularly polarized pulsed laser under resonant and off-resonant conditions, Chem. Phys. **324**, 367 (2006).

[4] N. V. Vitanov, A. A. Rangelov, B. W. Shore, and K. Bergmann, Stimulated Raman adiabatic passage in physics, chemistry, and beyond, Rev. Mod. Phys. **89**, 015006 (2017).

[5] C. P. Koch, M. Lemeshko, and D. Sugny, Quantum control of molecular rotation, Rev. Mod. Phys. **91**, 035005 (2019).

[6] D. Guéry-Odelin, A. Ruschhaupt, A. Kiely, E. Torrontegui, S. Martínez-Garaot, and J. G. Muga, Shortcuts to adiabaticity: Concepts, methods, and applications, Rev. Mod. Phys. **91**, 045001 (2019).

[7] D. Stefanatos and E. Paspalakis, A shortcut tour of quantum control methods for modern quantum technologies, Europhys. Lett. **132**, 60001 (2020).

[8] H. Singh, F. E. Berggötz, W. Sun, and M. Schnell, Chiral control of gas-phase molecules using microwave pulses, Angew. Chem. Int. Ed. **62**, e202219045 (2023).

[9] M. E. Franks, G. R. Macpherson, and W. D. Figg, Thalidomide, The Lancet **363**, 1802 (2004).

[10] P. G. Mezey, *New Developments in Molecular Chirality* (Springer Science & Business Media, Berlin, 2012), Vol. 5.

[11] R. Baron and J. A. McCammon, Molecular recognition and ligand association, Annu. Rev. Phys. Chem. **64**, 151 (2013).

[12] N. Berova, K. Nakanishi, and R. W. Woody, *Circular Dichroism: Principles and Applications* (John Wiley & Sons, New York, 2000).

[13] L. D. Barron, *Molecular Light Scattering and Optical Activity* (Cambridge University, Cambridge, 2009).

[14] K. W. Busch and M. A. Busch, *Chiral Analysis* (Elsevier, New York, 2011).

[15] L. A. Nafie, *Vibrational Optical Activity: Principles and Applications* (John Wiley & Sons, New York, 2011).

[16] C. Ye, Y. Sun, Y. Li, and X. Zhang, Single-shot nondestructive quantum sensing for gaseous samples with hundreds of chiral molecules, J. Phys. Chem. Lett. **14**, 6772 (2023).

[17] I. Erez, E. R. Wallach, and Y. Shagam, Simultaneous enantiomer-resolved Ramsey spectroscopy scheme for chiral molecules, Phys. Rev. X **13**, 041025 (2023).

[18] P. Král and M. Shapiro, Cyclic population transfer in quantum systems with broken symmetry, Phys. Rev. Lett. **87**, 183002 (2001).

[19] D. Gerbasi, M. Shapiro, and P. Brumer, Theory of enantiomeric control in dimethylallene using achiral light, J. Chem. Phys. **115**, 5349 (2001).

[20] P. Král, I. Thanopulos, M. Shapiro, and D. Cohen, Two-step enantio-selective optical switch, Phys. Rev. Lett. **90**, 033001 (2003).

[21] I. Thanopulos, P. Král, and M. Shapiro, Theory of a two-step enantiomeric purification of racemic mixtures by optical means: The D_2S_2 molecule, J. Chem. Phys. **119**, 5105 (2003).

[22] Y. Li, C. Bruder, and C. P. Sun, Generalized Stern-Gerlach effect for chiral molecules, Phys. Rev. Lett. **99**, 130403 (2007).

[23] E. Hirota, Triple resonance for a three-level system of a chiral molecule, Proc. Jpn. Acad. Ser. B **88**, 120 (2012).

[24] D. Patterson, M. Schnell, and J. M. Doyle, Enantiomer-specific detection of chiral molecules via microwave spectroscopy, Nature (London) **497**, 475 (2013).

[25] D. Patterson and J. M. Doyle, Sensitive chiral analysis via microwave three-wave mixing, Phys. Rev. Lett. **111**, 023008 (2013).

[26] D. Patterson and M. Schnell, New studies on molecular chirality in the gas phase: Enantiomer differentiation and determination of enantiomeric excess, Phys. Chem. Chem. Phys. **16**, 11114 (2014).

[27] V. A. Shubert, D. Schmitz, D. Patterson, J. M. Doyle, and M. Schnell, Identifying enantiomers in mixtures of chiral molecules with broadband microwave spectroscopy, Angew. Chem. Int. Ed. **53**, 1152 (2014).

[28] V. A. Shubert, D. Schmitz, C. Medcraft, A. Krin, D. Patterson, J. M. Doyle, and M. Schnell, Rotational spectroscopy and three-wave mixing of 4-carvomenthenol: A technical guide to measuring chirality in the microwave regime, J. Chem. Phys. **142**, 214201 (2015).

[29] S. Lobsiger, C. Pérez, L. Evangelisti, K. K. Lehmann, and B. H. Pate, Molecular structure and chirality detection by Fourier transform microwave spectroscopy, J. Phys. Chem. Lett. **6**, 196 (2015).

[30] V. A. Shubert, D. Schmitz, C. Pérez, C. Medcraft, A. Krin, S. R. Domingos, D. Patterson, and M. Schnell, Chiral analysis using broadband rotational spectroscopy, J. Phys. Chem. Lett. **7**, 341 (2016).

[31] C. Ye, Q. Zhang, Y.-Y. Chen, and Y. Li, Determination of enantiomeric excess with chirality-dependent ac Stark effects in cyclic three-level models, Phys. Rev. A **100**, 033411 (2019).

[32] M. R. Cai, C. Ye, H. Dong, and Y. Li, Enantiodetection of chiral molecules via two-dimensional spectroscopy, Phys. Rev. Lett. **129**, 103201 (2022).

[33] M. Khokhlova, E. Pisanty, S. Patchkovskii, O. Smirnova, and M. Ivanov, Enantiosensitive steering of free-induction decay, Sci. Adv. **8**, eabq1962 (2022).

[34] S. Eibenberger, J. Doyle, and D. Patterson, Enantiomer-specific state transfer of chiral molecules, Phys. Rev. Lett. **118**, 123002 (2017).

[35] C. Pérez, A. L. Steber, S. R. Domingos, A. Krin, D. Schmitz, and M. Schnell, Coherent enantiomer-selective population enrichment using tailored microwave fields, Angew. Chem. Int. Ed. **56**, 12512 (2017).

[36] J. H. Lee, J. Bischoff, A. O. Hernandez-Castillo, B. Sartakov, G. Meijer, and S. Eibenberger-Arias, Quantitative study of enantiomer-specific state transfer, Phys. Rev. Lett. **128**, 173001 (2022).

[37] J. Lee, E. Abdiha, B. G. Sartakov, G. Meijer, and S. Eibenberger-Arias, Near-complete chiral selection in rotational quantum states, Nat. Commun. **15**, 7441 (2024).

[38] D. Patterson and J. M. Doyle, Cooling molecules in a cell for FTMW spectroscopy, Mol. Phys. **110**, 1757 (2012).

[39] N. R. Hutzler, H.-I. Lu, and J. M. Doyle, The buffer gas beam: An intense, cold, and slow source for atoms and molecules, Chem. Rev. **112**, 4803 (2012).

[40] D. Patterson, Method for preparation and readout of polyatomic molecules in single quantum states, Phys. Rev. A **97**, 033403 (2018).

[41] Y. Li and C. Bruder, Dynamic method to distinguish between left- and right-handed chiral molecules, Phys. Rev. A **77**, 015403 (2008).
[42] M. Leibscher, T. F. Giesen, and C. P. Koch, Principles of enantio-selective excitation in three-wave mixing spectroscopy of chiral molecules, J. Chem. Phys. **151**, 014302 (2019).
[43] J.-L. Wu, Y. Wang, J. Song, Y. Xia, S.-L. Su, and Y.-Y. Jiang, Robust and highly efficient discrimination of chiral molecules through three-mode parallel paths, Phys. Rev. A **100**, 043413 (2019).
[44] C. Ye, Q. Zhang, Y.-Y. Chen, and Y. Li, Effective two-level models for highly efficient inner-state enantioseparation based on cyclic three-level systems of chiral molecules, Phys. Rev. A **100**, 043403 (2019).
[45] J.-L. Wu, Y. Wang, J.-X. Han, C. Wang, S.-L. Su, Y. Xia, Y. Jiang, and J. Song, Two-path interference for enantiomer-selective state transfer of chiral molecules, Phys. Rev. Appl. **13**, 044021 (2020).
[46] B. Liu, C. Ye, C. P. Sun, and Y. Li, Enantiospecific state transfer for gaseous symmetric-top chiral molecules, Phys. Rev. A **105**, 043110 (2022).
[47] N. V. Vitanov and M. Drewsen, Highly efficient detection and separation of chiral molecules through shortcuts to adiabaticity, Phys. Rev. Lett. **122**, 173202 (2019).
[48] J.-J. Cheng, C. Ye, and Y. Li, Enantio-specific state transfer of chiral molecules through enantio-selective shortcut-to-adiabaticity paths, J. Chem. Phys. **158**, 164303 (2023).
[49] B. T. Torosov, M. Drewsen, and N. V. Vitanov, Efficient and robust chiral resolution by composite pulses, Phys. Rev. A **101**, 063401 (2020).
[50] B. T. Torosov, M. Drewsen, and N. V. Vitanov, Chiral resolution by composite Raman pulses, Phys. Rev. Res. **2**, 043235 (2020).
[51] Y. Guo, X. Gong, S. Ma, and C.-C. Shu, Cyclic three-level-pulse-area theorem for enantioselective state transfer of chiral molecules, Phys. Rev. A **105**, 013102 (2022).
[52] M. Leibscher, E. Pozzoli, C. Pérez, M. Schnell, M. Sigalotti, U. Boscain, and C. P. Koch, Full quantum control of enantiomer-selective state transfer in chiral molecules despite degeneracy, Commun. Phys. **5**, 110 (2022).
[53] X. Gong, Y. Guo, C. Wang, X. Luo, and C.-C. Shu, Discrimination of enantiomers for chiral molecules using analytically designed microwave pulses, Phys. Chem. Chem. Phys. **24**, 18722 (2022).
[54] H. Xu, X.-K. Song, L. Ye, and D. Wang, Efficient and robust chiral discrimination by invariant-based inverse engineering, Opt. Lett. **48**, 2684 (2023).
[55] J.-J. Cheng, L. Du, Y. Li, and N. Zhao, Robust and high-efficiency dynamical method of enantio-specific state transfer, Opt. Express **32**, 8684 (2024).
[56] B. Liu, Y. Li, C. Ye, and C. Sun, Pump-control approach to enantiospecific state transfer, Opt. Express **32**, 28282 (2024).
[57] J. M. Horowitz and K. Jacobs, Energy cost of controlling mesoscopic quantum systems, Phys. Rev. Lett. **115**, 130501 (2015).
[58] O. Abah, R. Puebla, A. Kiely, G. De Chiara, M. Paternostro, and S. Campbell, Energetic cost of quantum control protocols, New J. Phys. **21**, 103048 (2019).
[59] T. Huang, Y. Ban, E. Y. Sherman, and X. Chen, Machine-learning-assisted quantum control in a random environment, Phys. Rev. Appl. **17**, 024040 (2022).
[60] L. Garcia, J. M. Bofill, I. d. P. Moreira, and G. Albareda, Highly adiabatic time-optimal quantum driving at low energy cost, Phys. Rev. Lett. **129**, 180402 (2022).
[61] U. Boscain, M. Sigalotti, and D. Sugny, Introduction to the Pontryagin maximum principle for quantum optimal control, PRX Quantum **2**, 030203 (2021).
[62] R. Rodriguez, B. Ahmadi, G. Suárez, P. Mazurek, S. Barzanjeh, and P. Horodecki, Optimal quantum control of charging quantum batteries, New J. Phys. **26**, 043004 (2024).
[63] V. Evangelakos, E. Paspalakis, and D. Stefanatos, Fast charging of an Ising-spin-pair quantum battery using optimal control, Phys. Rev. A **110**, 052601 (2024).
[64] D. P. Pires, M. Cianciaruso, L. C. Céleri, G. Adesso, and D. O. Soares-Pinto, Generalized geometric quantum speed limits, Phys. Rev. X **6**, 021031 (2016).
[65] M. M. Taddei, B. M. Escher, L. Davidovich, and R. L. de Matos Filho, Quantum speed limit for physical processes, Phys. Rev. Lett. **110**, 050402 (2013).
[66] A. del Campo, I. L. Egusquiza, M. B. Plenio, and S. F. Huelga, Quantum speed limits in open system dynamics, Phys. Rev. Lett. **110**, 050403 (2013).
[67] S. Campbell and S. Deffner, Trade-off between speed and cost in shortcuts to adiabaticity, Phys. Rev. Lett. **118**, 100601 (2017).
[68] L.-B. Fan, C.-C. Shu, D. Dong, J. He, N. E. Henriksen, and F. Nori, Quantum coherent control of a single molecular-polariton rotation, Phys. Rev. Lett. **130**, 043604 (2023).
[69] Q.-Q. Hong, Z.-Z. Lian, C.-C. Shu, and N. E. Henriksen, Quantum control of field-free molecular orientation, Phys. Chem. Chem. Phys. **25**, 32763 (2023).
[70] Q.-Q. Hong, D. Dong, N. E. Henriksen, F. Nori, J. He, and C.-C. Shu, Precise quantum control of molecular rotation toward a desired orientation, Phys. Rev. Res. **7**, L012049 (2025).
[71] L.-B. Fan, H.-J. Li, Q. Chen, H. Zhou, H. Liu, and C.-C. Shu, Maximizing orientation of a three-state molecule in a cavity with analytically designed pulses, Phys. Rev. A **111**, 033119 (2025).
[72] C. Ye, Q. Zhang, and Y. Li, Real single-loop cyclic three-level configuration of chiral molecules, Phys. Rev. A **98**, 063401 (2018).
[73] Y.-Y. Chen, C. Ye, Q. Zhang, and Y. Li, Enantio-discrimination via light deflection effect, J. Chem. Phys. **152**, 204305 (2020).
[74] Q. Zhang, Y.-Y. Chen, C. Ye, and Y. Li, Evading thermal population influence on enantiomeric-specific state transfer based on a cyclic three-level system via ro-vibrational transitions, J. Phys. B: At. Mol. Opt. Phys. **53**, 235103 (2020).
[75] P. M. Poggi, G. De Chiara, S. Campbell, and A. Kiely, Universally robust quantum control, Phys. Rev. Lett. **132**, 193801 (2024).
[76] A. Norambuena, M. Mattheakis, F. J. González, and R. Coto, Physics-informed neural networks for quantum control, Phys. Rev. Lett. **132**, 010801 (2024).